High-mass dimuon production in $\bar{p}N$ and $\pi^- N$ interactions at 125 GeV/c

E. Anassontzis, S. Katsanevas, E. Kiritsis, C. Kourkoumelis, A. Markou, L. K. Resvanis, and G. Voulgaris
University of Athens, Athens, Greece

M. Binkley, B. Cox, J. Enagonio,* C. Hojvat, D. Judd,† R. D. Kephart, P. K. Malhotra,‡ P. O. Mazur, C. T. Murphy, F. Turkot, R. L. Wagner, D. Wagoner,† and W. Yang
Fermi National Accelerator Laboratory, Batavia, Illinois 60510

H. Areti,§ S. Conetti, P. Lebrun,§ D. G. Ryan, T. Ryan,** W. Schappert,†† and D. G. Stairs
McGill University, Montreal, Quebec, Canada H3A 2T8

C. Akerlof, X. Cui,‡‡ P. Kraushaar,§§ D. Nitz, R. Thun, and L. Wang‡‡
University of Michigan, Ann Arbor, Michigan 48109

He Mao and Zhang Nai-jian
Shandong University, Jinan, Shandong, People's Republic of China
(Received 19 January 1988)

We have studied muon pairs with an invariant mass between 4 and 9 GeV/c^2 produced in $\bar{p}N$ and $\pi^- N$ interactions at an incident momentum of 125 GeV/c. The experiment was performed at Fermilab using a tungsten target and a special beam enriched to contain 18% antiprotons. We compare differential distributions as functions of the dimuon invariant mass, Feynman x, transverse momentum, and decay angles of the dimuon to the predictions of the Drell-Yan model including QCD corrections. Quark structure functions for the $\bar{p}$ and π^- are extracted. Comparisons of the antiproton data to the Drell-Yan model are significant because the cross sections depend principally on the valence-quark structure functions which are accurately determined by deep-inelastic scattering measurements. The measured absolute cross section (integrated over positive Feynman x and all transverse momenta) is $0.106\pm0.005\pm0.008$ nb/nucleon for the $\bar{p}N$ interaction and $0.107\pm0.003\pm0.009$ nb/nucleon for the $\pi^- N$ interaction, where the quoted errors are statistical and systematic, respectively. Normalization (K) factors that are required to bring the naive Drell-Yan and first-order QCD predictions into agreement with the measurements are extracted, and the uncertainties involved in such comparisons are examined.

I. INTRODUCTION

The comparison of experimental data with the predictions of the Drell-Yan mechanism for high-mass lepton pair production in hadronic collisions provides a stringent test of simple quark-parton model ideas and the various QCD extensions required.[1-3] A study of the process $\bar{p}N \to \mu^+\mu^- X$ is particularly valuable because the cross section for this reaction is dominated by the annihilation of valence quarks and antiquarks whose structure functions have been accurately determined in deep-inelastic lepton scattering (DIS) experiments.[4] Figure 1 shows the Feynman diagrams for the Drell-Yan process and its first-order QCD corrections. In the leading-log approximation of QCD, the cross section for hadronic muon pair production, integrated over the transverse momentum p_T of the dimuon, is given by[5]

$$\frac{d^2\sigma}{dM\,dx_F} = \frac{8\pi\alpha^2(1-\tau)}{9M^3[x_F^2(1-\tau)^2+4\tau]^{1/2}} \times \sum_{q=u,d,s} e_q^2[\bar{q}^{\,B}(x_1,Q^2)q^{\,T}(x_2,Q^2) + q^{\,B}(x_1,Q^2)\bar{q}^{\,T}(x_2,Q^2)] \,. \quad (1)$$

Here M is the invariant mass of the muon pair, $\tau = M^2/s = x_1 x_2$, $x_F = 2p_L/[\sqrt{s}\,(1-\tau)]$ is the ratio of the longitudinal momentum of the pair to the maximum allowable momentum in the center-of-mass frame, e_q is the quark charge, x_1 (x_2) is the momentum fraction of the beam (target) particle carried by the interacting quark, and the $q(x,Q^2)$'s are the beam (B) and target (T) quark structure functions of the interacting hadrons. The quark structure functions should be identical to those measured in deep-inelastic lepton scattering experiments at spacelike values of Q^2 which are continued to the timelike region by making the identification $Q^2 = M^2$. Theoretical studies[6] have shown that the Drell-Yan cross section factorizes into functions of x_1 and x_2 to second order in QCD, reaffirming the validity of (1).

First-order QCD corrections[7] [Figs. 1(b)–1(d)] are expected to increase the observed cross section over that of (1) by a factor which is constant to $\pm 10\%$ in the region of x_1 and x_2 probed by current experiments ($0.1 < x_{1,2} < 0.9$). This "K factor" is substantial (1.5–2.5) and, within $\pm 25\%$, roughly independent of particle type. The first-order QCD annihilation and Compton diagrams also contribute to the p_T of the dimuon. However, calculations using these diagrams require an unrealistically large

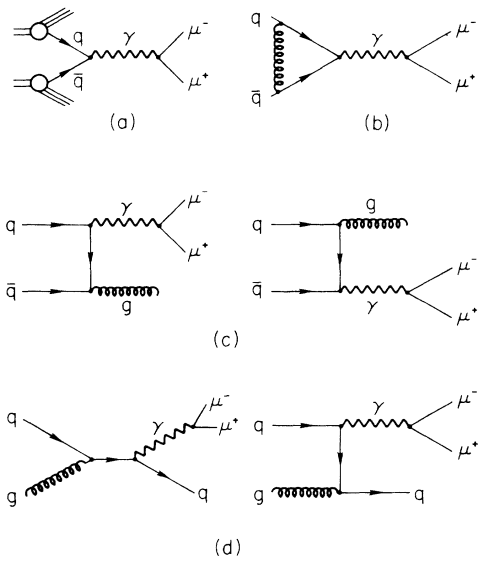

FIG. 1. Feynman diagrams for (a) simple Drell-Yan, (b) the vertex term, (c) the annihilation terms, and (d) the Compton terms.

value of the quark intrinsic p_T in order to fit existing pion and proton data, and (particularly in the case of the pion) predict too small an increase of $\langle p_T^2 \rangle$ with s (Ref. 8). The perturbative calculation of annihilation and Compton diagrams is, in fact, only valid for $p_T \geq M$, while most of the data exists at much lower values of p_T. Calculations[9] which include the effects of soft-gluon emission predict p_T distributions which require only modest values of intrinsic p_T [$\langle p_T^2 \rangle_{\text{int}} < 0.5$ (GeV/c)^2] to reproduce the pion and proton data. These soft-gluon graphs only slightly alter[9] the first-order K factor in the region of the scaling variable τ probed by current experiments.

The primary goal of the present experiment is a comparison of the reaction $\bar{p}N \to \mu^+\mu^- X$ with (1) and with higher-order corrections calculated using quark structure functions measured in DIS. Data from the reaction $\pi^- N \to \mu^+\mu^- X$ are used to make detailed scaling checks of $M^3 d\sigma/dM\, dx_F$ as functions of τ and x_F by comparing with data from other experiments at different energies. Quark structure functions are extracted from both the $\bar{p}$ and π^- data, and a best estimate of the K factor in the pion reaction is made via this procedure. The measured p_T distributions are compared to the QCD predictions, and the decay-angular distributions of the dimuon are checked for consistency with the naive Drell-Yan model.

II. APPARATUS AND EVENT RECONSTRUCTION

A detailed description of the beam, experimental apparatus, and event reconstruction can be found elsewhere.[10] The experiment used a special tertiary beam of mean momentum 125 GeV/c and composed of 18% antiprotons and 82% pions resulting from $\bar{\Lambda}^0$, Λ^0, and K_S^0 decays. The experiment normally operated at a beam intensity of 1.5×10^7 particles/sec. Incident pions as well as incident antiprotons were tagged by Cherenkov counters, resulting in less than 0.5% pion contamination of the antiproton data. Beam hodoscopes and proportional chambers were used to measure the trajectory and momentum of each incident beam particle.

Figure 2 shows the experimental spectrometer which included a tungsten target, a 10.3-absorption-length copper hadron absorber, 20 proportional- and drift-chamber planes, a large-aperture analysis magnet, a two-layer x-y charged-particle scintillation-counter hodoscope (180 elements), and a 13.2-absorption-length steel and concrete muon detector with three scintillation-counter hodoscope muon-trigger planes of 60 elements each. At different times, data were taken with targets of thickness 0.416, 0.998, and 1.50 $\bar{p}$ absorption lengths. The individual elements of the muon hodoscope planes were aligned so that a threefold coincidence between planes would point back to the target. The fast dimuon trigger required two threefold coincidences in the three muon hodoscope planes, at least two hits in the charged-particle scintillation-counter hodoscope, and a $\bar{p}$ or π^- signal from the beam tagging system. The π^- signal was sometimes prescaled in order to reduce the dead time due to event read out. Events which produced a fast trigger were sent to an ECL-CAMAC trigger processor.[11] The processor used hits (within fiducial regions defined by the threefold coincidences) from the drift chambers downstream of the analysis magnet to calculate the momenta of muon candidates and subsequently the masses of all possible muon pairs in less than 10 μsec. Events with dimuon candidates of invariant mass greater than 2.0 GeV/c^2 were recorded on magnetic tape.

The off-line analysis program reconstructed track segments in the drift chambers both upstream and downstream of the magnet and assumed a horizontal bend plane at the magnetic center to determine the momentum for matching segments. The 250-μm measured resolution of the drift chambers and the measured field integral of 2766 kG cm resulted in a momentum resolution of $\Delta p/p = 0.004p$. This momentum resolution contributed a negligible amount to the observed ψ mass resolution, which was dominated by uncertainty in the dimuon opening-angle measurement due to multiple scattering in the target and hadron absorber.

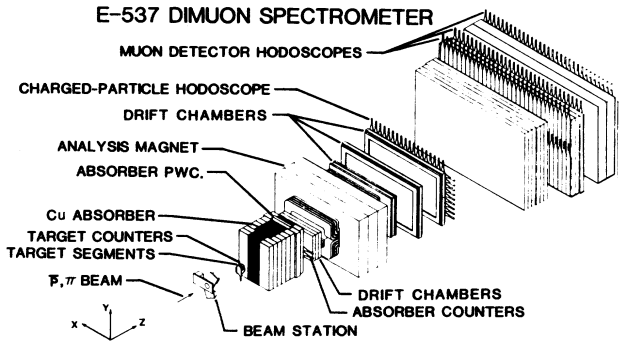

FIG. 2. General layout of the spectrometer used by E537 to measure high-mass dimuon production. The coordinate system used is indicated where the y direction is vertical.

Events which had at least two muon candidates with an invariant mass greater than 2.0 GeV/c^2 were subject to a second stage of reconstruction. Information from the beam chambers was used to determine the four-momentum of the incident beam particle causing the interaction. This was combined with track coordinates from the upstream drift chambers and the multiwire proportional chamber (MWPC) placed inside the hadron absorber in order to distinguish events originating in the target from events originating in the dump using an algorithm similar to that of Ref. 12. The positions and angles of the muons as they exited from the absorber and the positions of the muons as measured by the absorber MWPC were used to calculate a probability function which depended on the vertex coordinates of the event and the initial angles of the muons before they entered the absorber. The probability function, which included measurement errors and multiple scattering in the absorber, was maximized as a function of the z coordinate of the vertex and the initial angles of the muons. The transverse coordinates of the interaction vertex were determined from the reconstructed incident beam track. The z coordinate distribution resulting from this fitting procedure is shown in Fig. 3 for the 1.5-$\bar{p}$-absorption-length (14.71-cm) tungsten target. The cuts used in the analysis are indicated by dashed lines.

Requirements were also placed on the distance between the two tracks at the reconstructed vertex and on the transverse position of the vertex in order to help reject muon pairs which were the result of an accidental coincidence between a beam halo particle and a muon from the decay of a hadron. The reconstructed vertex was required to be within ± 9.144 cm in x and ± 10.16 cm in y of the nominal beam center at the target. The Monte Carlo simulation showed that the longitudinal and transverse vertex requirements caused a loss of less than 1% of the real events with no bias as a function of any kinematic variable.

Events which reconstructed to the target region were reanalyzed assuming that the z coordinate of the production vertex was at the center of the target. This procedure improved the ψ mass resolution for the 1.5-absorption-length tungsten target from $\sigma = 270$ MeV/c^2 to $\sigma = 185$ MeV/c^2. The improved resolution for the 0.5-absorption-length tungsten target was $\sigma = 140$ MeV/c^2. The invariant-mass spectra for both like-sign and opposite-sign dimuons produced in $\bar{p}$ and π^- interactions in the 1.5-absorption-length target are shown in Figs. 4(a) and 4(b), respectively. Table I gives the in-

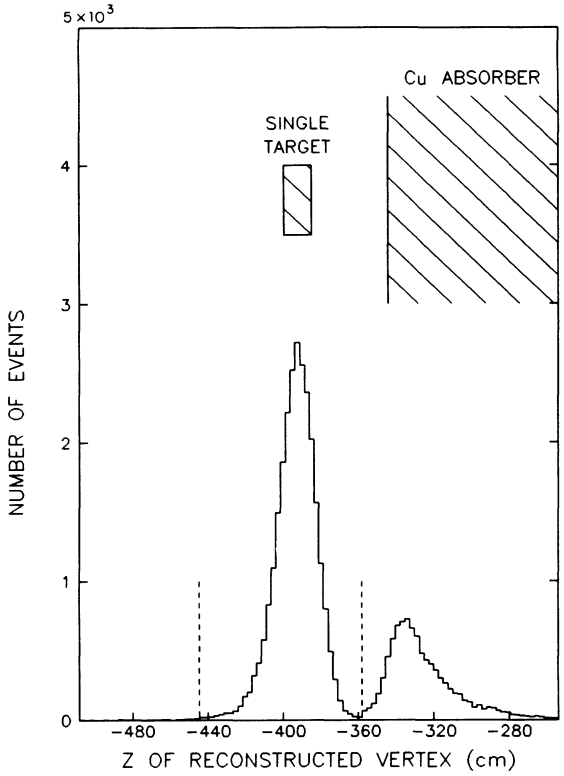

FIG. 3. Reconstructed dimuon vertex positions for the 1.5-absorption-length tungsten target. The cuts used in the analysis are indicated.

TABLE I. Data from tungsten targets. For the tungsten targets used in E537, the table gives the number of absorption lengths, the integrated incident beams, the number of recorded events with $4 < M < 9$ GeV/c^2, and the reinteraction correction for the (a) $\bar{p}$ and (b) π^- beam components. Note that the second target listed was actually two equal segments separated sufficiently in z so that data from the upstream target could be isolated and used in the ψ reinteraction measurement (see Fig. 6).

Target length (cm)	No. of absorption lengths	Integrated beam (10^{-11})	Events $4 < M < 9$ GeV/c^2	Reinteraction correction factor
		(a) $\bar{p}$		
4.087	0.416	0.1536	14	0.984±0.009
2×4.905	0.998	0.7792	106	0.966±0.019
14.710	1.50	1.415	267	0.954±0.022
Total		2.348	387	
		(b) π^-		
4.087	0.343	0.7060	54	0.987±0.007
2×4.905	0.823	2.014	367	0.971±0.016
14.710	1.234	3.232	680	0.960±0.022
Total		5.952	1101	

tegrated $\bar{p}$ and π^- beam fluxes and number of reconstructed events in the high-mass continuum region ($4 < M < 9$ GeV/c^2) for each target.

III. CORRECTIONS TO THE DATA

Corrections were applied to the data for trigger processor inefficiency (1%), for scintillation counter inefficiency and gaps between adjacent counters (10%), and for vertex cut inefficiency (1%) (Ref. 10). This section covers the additional corrections for muon energy loss in the spectrometer, for contamination by random muon pairs, for ψ and ψ' resonance tails in the high-mass continuum region, and for reinteraction in the target. The corrections for Fermi motion and track-finding inefficiency were incorporated into the Monte Carlo acceptance program, which is the topic of Sec. IV.

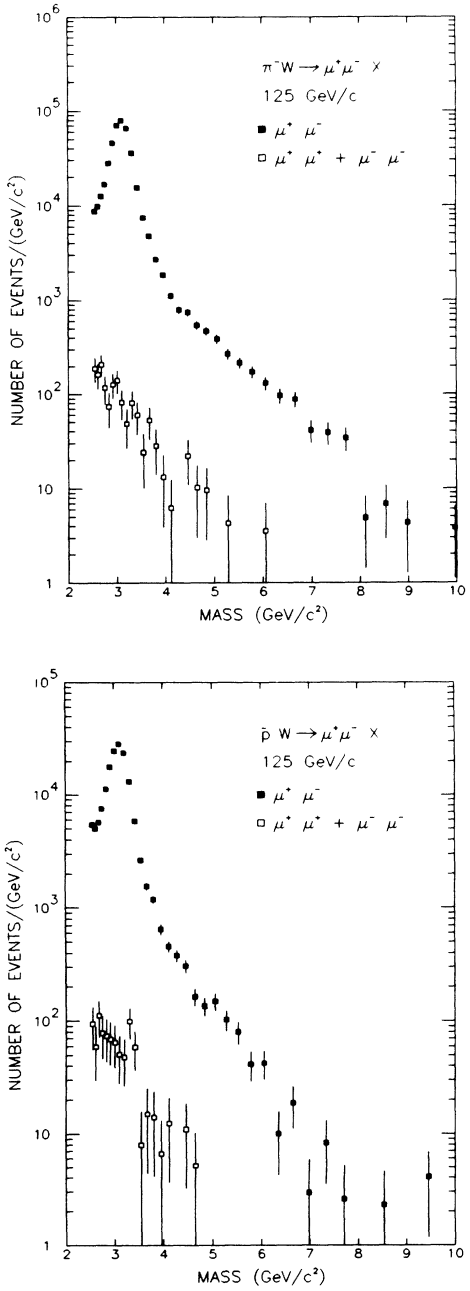

FIG. 4. Uncorrected dimuon mass spectrum produced by $\bar{p}$ and π^- incident on a tungsten target at 125 GeV/c. The background level is shown by like-sign targets. The ψ resonance is seen at 3.1 GeV/c^2.

A. Muon energy loss in the spectrometer

Muon track momenta were corrected on average for energy loss in the tungsten target and copper absorber using tables calculated from the Bethe-Bloch ionization formula with corrections for density effects, bremsstrahlung, and nuclear interactions.[13,14] The Monte Carlo program which simulated the acceptance and trigger logic included corrections for muon energy loss in the target, copper absorber, and concrete and steel muon filter. The calculated values of mean energy loss for tungsten, copper, beryllium, iron, and concrete were parametrized for kinetic energies between 100 MeV and 125 GeV, and are plotted in Fig. 5. The parametrization for iron was compared with other calculations in the literature[15,16] and all were found to agree to better than 1% for muon energies in the range of interest.

B. Contamination by random muon pairs

The number of like-sign events with masses between 4 and 9 GeV/c^2 is 1.5% of the opposite-sign sample in both the $\bar{p}$ and π^- data (Fig. 4). All of the like-sign events between 4 and 9 GeV/c^2 are negatively charged muon pairs

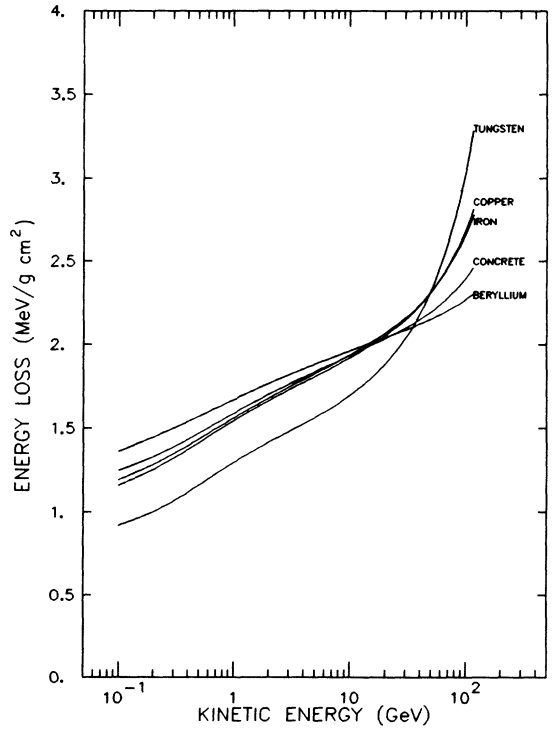

FIG. 5. The energy loss for muons in the various materials used in the spectrometer is shown as functions of the kinetic energy of the muon.

produced by random coincidences between one relatively high-momentum (between 20 and 125 GeV/c) halo muon which passed through the beam hole in the halo veto counters[10] and a low-momentum (less than 10 GeV/c) muon from the decay of a pion or kaon which was produced in an interaction in the target.

By studying events with vertices outside the cuts used to define true dimuon events, we found that the number of random events observed with a positive decay muon accompanying the negative beam halo muon was equal within statistics to the similar sample with two negative muons. In all the distributions presented in this paper, we therefore corrected our opposite-sign event sample by subtracting from it the like-sign events. The number of like-sign events was limited to 1.5% by using the vertex cuts and by rejecting events with a muon of momentum greater than 85 GeV/c (Ref. 17). The 85-GeV/c cut introduces a slight bias against events with very high x_F, but this was taken into account by making an identical cut in the Monte Carlo acceptance program. All accidental events fall near $\cos\theta = -1$, where the acceptance for true dimuon events is small (see Sec. IX).

C. Contamination by the ψ and ψ' resonances

Fits to the mass region between 2.6 and 4.5 GeV/c^2 with Gaussians centered at the ψ and ψ' masses and an exponentially falling background gave a production ratio of $\psi'/\psi = 0.02 \pm 0.01$ for both the $\bar{p}$ and π^- data. Using the Gaussian fits, the contamination of the continuum above 4 GeV/c^2 by resonance tails was calculated to be negligible for the ψ and $(2.4 \pm 1.2)\%$ for the ψ'. Two checks were made to ensure that no significant non-Gaussian tails were introduced by the event reconstruction. First, the χ^2's of individual tracks from events at the ψ resonance and from events above 4 GeV/c^2 were compared and found to be identical. Second, simulated ψ and ψ' events were generated in the Monte Carlo acceptance program which included multiple scattering, real background tracks, and inefficiencies in the chambers, all of which may cause track distortions. These simulated events were reconstructed with the same programs that were used for data events and no evidence of a non-Gaussian tail was found.

D. Reinteraction in the target

The correction required for events produced by secondary interactions in the target was determined by comparing the cross sections for ψ's produced by pions from the different length tungsten targets. If tertiary interactions are ignored and the absorption cross section is assumed to be independent of energy, the measured cross section should depend on the length of the target as

$$\sigma_{\text{measured}} = \sigma_{\text{direct}} + \sigma_{\text{reint}} \left[1 - \frac{L/\lambda_{\text{abs}}}{\exp(L/\lambda_{\text{abs}}) - 1} \right],$$

where L is the physical length, λ_{abs} is the absorption length of the target material, σ_{direct} is the cross section that would be measured using an infinitesimally thin target, and σ_{reint} is a constant that depends on the details of the reinteraction but is independent of the target length. Measured cross sections for different length targets can therefore be used to obtain values for σ_{direct} and σ_{reint}. The relative cross sections for ψ production by pions are shown as a function of target length in Fig. 6. The curve is the result of the fit for σ_{reint} and σ_{direct}, the intercept at zero target length.

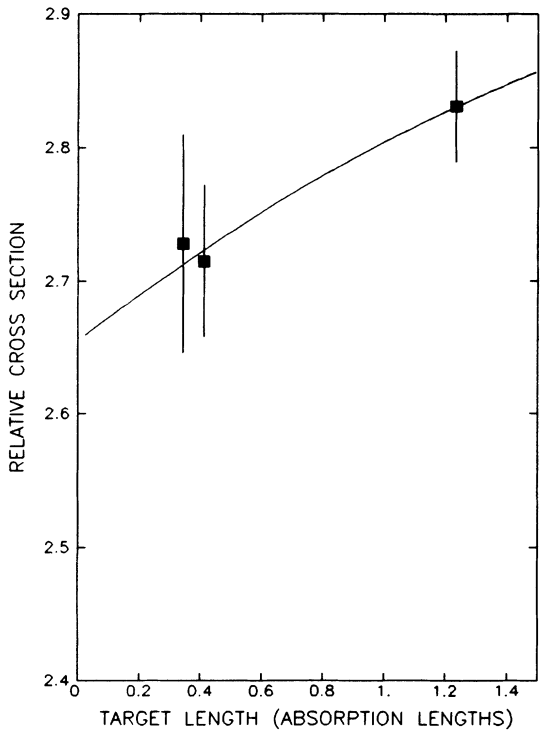

FIG. 6. Relative cross sections for ψ production by π^- as a function of tungsten target thickness. The increase with target thickness is due to reinteraction.

The Monte Carlo program CASIM (Ref. 18) was used to compare pion-produced ψ events and high-mass continuum events in order to estimate the reinteraction correction for the continuum region. CASIM uses the Hagedorn-Ranft thermodynamic model to generate a spectrum of secondary particles. The known τ dependences of the ψ and dimuon continuum cross sections[19] were used to generate muon pair events from this spectrum of secondaries. The muon pairs were propagated through the spectrometer using the Monte Carlo acceptance program, and a reinteraction rate for the high-mass continuum region was determined relative to that for ψ's produced by pions. Using these relative reinteraction rates and the measured reinteraction rate for ψ's produced by pions, correction factors were calculated for the continuum cross sections with various target and beam combinations and are given in Table I. The size of the overall correction is less than 5% for the high-mass antiproton-induced data and less than 4% for the pion data. Uncertainties in these corrections lead to an estimated 2% uncertainty in the final cross sections.

IV. MONTE CARLO ACCEPTANCE PROGRAM

The acceptance of the apparatus was calculated with a Monte Carlo program. Events were generated randomly throughout phase space using the measured beam energy spectrum and profile and allowing for Fermi motion of the target nucleon. The resulting pairs of muons were propagated through the spectrometer taking into account multiple scattering and energy loss. The track coordinates at the chambers were digitized, the counter hits were tagged, and the results were recorded in the same format used for the data tapes. Background hits in the chambers were included to produce the same track-finding efficiency as for real data events. The Monte Carlo events were then subject to the same set of analysis programs as the data, and both the initial and reconstructed values of the kinematic variables were saved. Using the maximum-likelihood method, the Monte Carlo events were fit to the unbinned data events and reweighted to accurately simulate the acceptance as a function of all kinematic variables.

A. Fermi-motion correction

The four-vector for the target nucleon was generated according to a simple Fermi gas model[20] to allow for motion of the nucleons inside the nucleus. The target nucleon was given an isotropic angular distribution in the laboratory frame and a momentum between 0 and the Fermi momentum distributed as $dN/dp = 3p^2/p^3_{\text{Fermi}}$. The Fermi momentum for the tungsten target was taken to be[21] $p_{\text{Fermi}} = 265$ MeV/c. High-momentum tails[22] in the Fermi distribution were investigated in the simulation and found to have no significant effect.

B. Track-finding efficiency

Background tracks which accompanied true dimuon events could be caused by beam halo particles or other interactions in the copper absorber. These sometimes produced inactive wires due to the 300-nsec discriminator dead time as well as background wire hits. Both effects were simulated in the Monte Carlo program by including drift chamber hits (and hence inactive wires) from special data runs taken using only the beam signal as a trigger.[17] Good agreement was observed between the backgrounds in reconstructed dimuon data events and the backgrounds in Monte Carlo–generated events which survived the reconstruction procedure. The overall efficiency for finding both tracks in a high-mass dimuon event was 90% and is shown as a function of M and x_F in Fig. 7. It is nearly constant over the measured range of all kinematic variables, the only exception being a decrease for large values of x_F. An overall systematic error of 4% is introduced by the track-finding correction.

C. Acceptance calculation and empirical fits to the data

The unbinned data events and reconstructed Monte Carlo events were used to fit the dependence of the cross section on the kinematic variables M, x_F, p_T, $\cos\theta$, and ϕ using the maximum-likelihood method.[23] The cross section (by which the Monte Carlo events were initially generated and thereafter reweighted) was parametrized as a product of simple functional forms of each variable and the fit found the set of parameters which maximized the probability of observing the experimental data points obtained. This was accomplished by maximizing the product of likelihood functions $L(x_i \mid \Gamma)$ for individual data events, that is,

$$L(x \mid \Gamma) = \prod_{i=1}^{N} L(x_i \mid \Gamma) ,$$

where N is the number of data events, $x_i = (M_i, x_{Fi}, p_{Ti}, \cos\theta_i, \phi_i)$ are the kinematic variables for the ith event, Γ represents the set of parameters being fit, and the likelihood function is defined by

$$L(x_i \mid \Gamma) = P(x_i \mid \Gamma) \left[\int P(x \mid \Gamma) dx \right]^{-1} ,$$

where $P(x_i \mid \Gamma)$ is the multidimensional functional form being fit to the data points. The denominator of the likelihood function was evaluated using the Monte Carlo events, which were reweighted at each step of the fit.

Good fits to both the $\bar{p}$ and π^- high-mass continuum data were obtained using the form

$$P(x \mid \Gamma) = P(M \mid \alpha_M) P(x_F \mid x_{F0}, \sigma_x) P(p_T \mid p_{T0}) \times P(\cos\theta \mid \lambda) P(\phi) ,$$

where

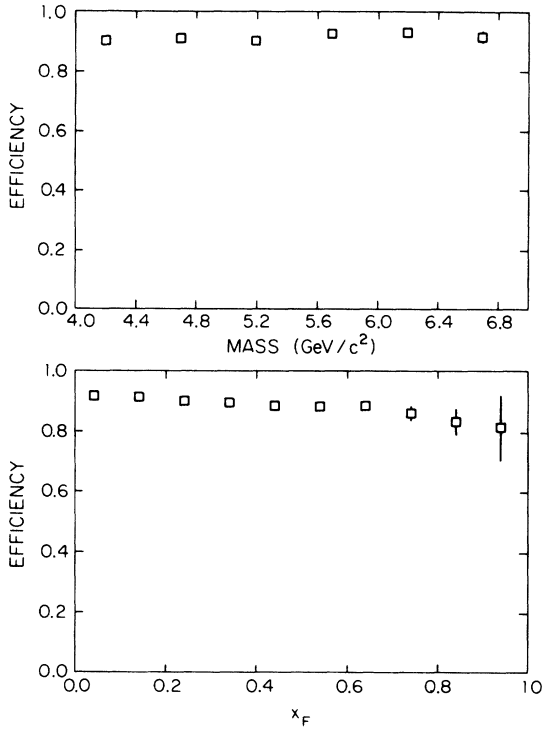

FIG. 7. The efficiency for finding both tracks in a high-mass dimuon event as functions of mass and x_F.

TABLE II. Kinematic distribution parameters. The fits to the data assuming that the $\cos(\theta)$ distribution behaves as (a) $1+\lambda\cos^2(\theta)$ with λ free and (b) $1+\cos^2(\theta)$. The acceptance A for each of the fits, and the gradient of the acceptance at the minimum of the negative log-likelihood function are also given.

Parameter	Value	Error	Correlation				Grad(A)
			(a) λ free				
Antiproton							
α_M	1.331	0.069					1.498×10^{-3}
x_{F0}	0.0	Fixed					
σ_x	0.608	0.020	0.021				1.542×10^{-1}
p_{T0}	1.107	0.028	0.022	0.034			-5.025×10^{-3}
λ	0.279	0.357	−0.074	−0.115	−0.217		-4.230×10^{-2}
A	0.237	0.022					
Pion							
α_M	1.116	0.036					-1.853×10^{-2}
x_{F0}	−0.032	0.080	−0.018				3.121×10^{-1}
σ_x	1.034	0.075	0.065	−0.929			7.571×10^{-3}
p_{T0}	1.158	0.018	0.023	0.019	−0.003		-3.114×10^{-3}
λ	1.130	0.285	−0.107	−0.120	0.058	−0.184	-2.647×10^{-2}
A	0.224	0.011					
			(b) λ fixed to 1				
Antiproton							
α_M	1.322	0.069					2.349×10^{-3}
x_{F0}	0.0	Fixed					
σ_x	0.604	0.019	0.014				1.433×10^{-1}
p_{T0}	1.097	0.027	0.003	0.013			2.897×10^{-3}
A	0.212	0.004					
Pion							
α_M	1.118	0.037					-2.150×10^{-3}
x_{F0}	−0.027	0.078	−0.031				3.130×10^{-2}
σ_x	1.032	0.074	0.072	−0.930			6.908×10^{-3}
p_{T0}	1.160	0.017	0.003	−0.004	0.008		-4.192×10^{-3}
A	0.227	0.003					

$$P(M\mid\alpha_M)=\alpha_M\exp(-\alpha_M M)[\exp(-\alpha_M M_{\min})-\exp(-\alpha_M M_{\max})]^{-1},$$

$$P(x_F\mid x_{F0},\sigma_x)=(\sqrt{2}/\pi)\exp(-0.5z^2)dz/dx_F,$$

with

$$z=(1/\sigma_x)\{\ln[(x_F+1)/(1-x_F)]-\ln[(x_{F0}+1)/(1-x_{F0})]\},$$

$$P(p_T\mid p_{T0})=2(p_T/p_{T0})(\sqrt{2}/\pi)\exp[-0.5(p_T/p_{T0})^2],$$

$$P(\cos\theta\mid\lambda)=\{1/[2(1+\lambda/3)]\}(1+\lambda\cos^2\theta),$$

and

$$P(\phi)=1/(2\pi).$$

The x_F distribution is a transformed Gaussian which vanishes at the kinematic limits: $x_F=\pm1$. The polar and azimuthal decay angles, θ and ϕ, of the positive muon were defined in the Gottfried-Jackson rest frame.[24] Tables II(a) and II(b) give the results of fits with λ free and with $\lambda=1$ as predicted by the Drell-Yan model. The fits with $\lambda=1$ were used to generate acceptances as functions of the kinematic variables as shown for the $\bar{p}$ data in Fig. 8. The acceptance for a bin from x_i to $x_i+\Delta x$ was defined as the ratio of the weighted number of accepted Monte Carlo events with a reconstructed value of x between x_i and $x_i+\Delta x$ to the weighted number of generated events with x between x_i and $x_i+\Delta x$. Calculating the acceptance in this manner compensated for smearing of the kinematic quantities due to Fermi motion of the target nucleon and apparatus resolution.

V. CROSS SECTIONS

The differential cross section for each value of the kinematic variable x was calculated using the formula

$$d\sigma/dx=(RN_{\text{events}})/(\Delta x\, N_0\rho L_{\text{eff}}\xi E N_{\text{beam}}),$$

where x is one of the kinematic variables (M, x_F, or p_T), $d\sigma/dx$ is the differential cross section in cm^2/nucleon assuming an A dependence of A^1, Δx is the width of the bin, A is the atomic mass of the target, N_0 is Avogadro's number, ρ is the density of the target in g/cm^3, L_{eff} is the effective length of the target, R is the correction for reinteraction and resonance contamination, ξ is the acceptance for the bin, E is the correction for counter and trigger efficiency, N_{events} is the number of data events in the bin, and N_{beam} is the number of beam particles hitting the target.

Before presenting the data, we will briefly describe the calculation of the effective length of the target and discuss the assumption that the cross section varies with the atomic mass of the target as A^1.

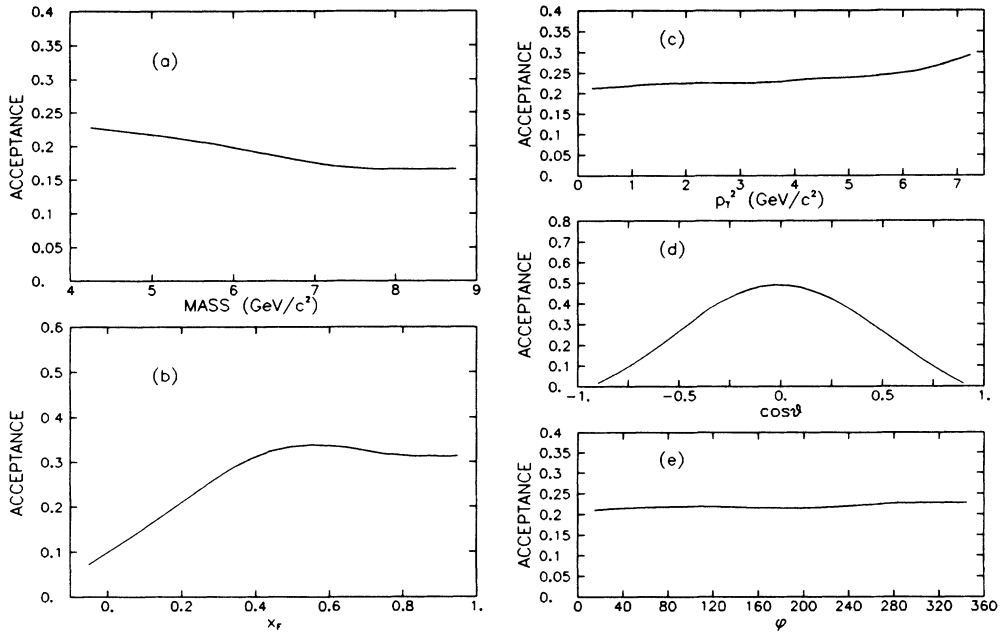

FIG. 8. Acceptance of the E537 spectrometer as a function of the muon pair kinematic variables (a) M, (b) x_F, (c) p_T^2, (d) $\cos\theta$, and (e) ϕ.

A. Effective length of the target

Each of the tungsten targets was carefully weighed and measured, and its effective length L_{eff} was calculated from

$$L_{\text{eff}}=\lambda_{\text{abs}}[1-\exp(-L/\lambda_{\text{abs}})] ,$$

where $\lambda_{\text{abs}}=\sigma_{\text{abs}}\rho N_0 A$ is the absorption length of the target material, L is the physical length of the target, and σ_{abs} is the absorption cross section. The absorption cross sections for antiproton and pion beams in tungsten were interpolated from measurements made at beam energies of 60 and 200 GeV (Ref. 25). The errors in the measured absorption cross sections contribute a 1.7% uncertainty to the effective lengths and thus to our quoted cross sections.

B. A dependence of the Drell-Yan cross section

As is well known, the total cross section for hadronic interactions in nuclei grows approximately as $A^{0.7}$. This is explained by the shadowing of the interior of the nucleus by the surface, and is thus dependent on the large strength of the hadronic interaction. In 1975 Farrar[26] proposed a model for strong interactions in nuclei which predicted that at high mass the Drell-Yan cross section should vary as A^1. The model assumed that the intrinsic strength of the strong interaction (i.e., the quark-gluon and gluon-gluon coupling) is small, with the apparent large strength of most hadronic processes being due to multiple interactions of quarks with small relative momenta over a long period of time. The fastest moving quarks will probably not interact and propagate freely through the nucleus. Infrequently, the fast quarks will annihilate to produce a high-mass muon pair. Farrar estimated that the threshold for A^1 behavior would occur in the dimuon mass range between 2 and 6 GeV/c^2.

Kenyon[2] has reviewed subsequent high-statistics A-dependence measurements using pion and proton beams. These measurements show that, for values of invariant mass greater than 4 GeV/c^2, the dimuon cross section increases as A^1 independent of M, x_F, and p_T in agreement with Farrar's prediction. From Kenyon's summary, we estimate the current experimental uncertainty in the power α of A^α to be $\pm 2\%$, which corresponds to a $\pm 11\%$ uncertainty in the cross section per nucleon extracted from tungsten data. A recent publication by the NA10 Collaboration[27] of very high statistics π^- data reports an overall A dependence consistent with $\alpha=1.00\pm 0.02$, but notes a decrease in the tungsten-to-deuterium production at high x_2 consistent with the European Muon Collaboration (EMC) effect in DIS. However, the effect is small compared to the statistical accuracy of our data at the relevant x_2 values. The error in the cross sections due to the uncertainty in the A-dependence correction will be indicated separately. Note that the cross sections given are per average nucleon which, for tungsten, is 40% proton and 60% neutron.

C. Data and overall systematic error

The differential cross sections as functions of M, x_F, and p_T^2 are shown in Fig. 9. Values of the double differential cross sections in terms of (M,x_F), (M,p_T^2), and (x_F,p_T^2) are given in Table III. The errors shown in the figures and table are statistical only. The total integrated cross sections for $x_F>0$, all p_T, and $4<M<9$ GeV/c^2 are $0.106\pm 0.005\pm 0.008$ nb/nucleon for the $\bar{p}$-induced reaction and $0.107\pm 0.003\pm 0.009$ nb/nucleon for the π^--induced reaction. The first error quoted is sta-

TABLE III. Double-differential dimuon cross sections in (M,x_F), (M,p_T^2), and (x_F,p_T^2) for the $\bar{p}N$ and $\pi^- N$ data at 125 GeV/c. The entries were extracted from data from tungsten targets using an assumed dependence on the atomic mass of the target of A^1. The cross sections are in units of nb/nucleon (variable units). Mass is in units of GeV/c^2 and p_T^2 is in units of (GeV/c)^2. The statistical uncertainty in each value is listed immediately below the cross section.

x_F \ Mass	4.0–4.5	4.5–5.0	5.0–5.5	5.5–6.0	$\bar{p}$ 6.0–6.5	6.5–7.0	7.0–7.5	7.5–8.0	8.0–8.5	8.5–9.0
−0.1–0.0	0.331×10^{0}	0.194×10^{0}	0.917×10^{-1}	0.593×10^{-1}	0.000×10^{0}	0.000×10^{0}	0.000×10^{0}	0.000×10^{0}	0.000×10^{0}	0.000×10^{0}
	0.792×10^{-1}	0.594×10^{-1}	0.379×10^{-1}	0.301×10^{-1}	0.169×10^{-1}	0.157×10^{-1}	0.145×10^{-1}	0.978×10^{-2}	0.143×10^{-1}	0.122×10^{-1}
0.0–0.1	0.271×10^{0}	0.145×10^{0}	0.655×10^{-1}	0.373×10^{-1}	0.102×10^{-1}	0.102×10^{-1}	0.976×10^{-2}	0.000×10^{0}	0.000×10^{0}	0.000×10^{0}
	0.527×10^{-1}	0.394×10^{-1}	0.270×10^{-1}	0.189×10^{-1}	0.103×10^{-1}	0.103×10^{-1}	0.995×10^{-2}	0.949×10^{-2}	0.154×10^{-1}	0.872×10^{-2}
0.1–0.2	0.237×10^{0}	0.779×10^{-1}	0.887×10^{-1}	0.628×10^{-1}	0.650×10^{-2}	0.192×10^{-1}	0.000×10^{0}	0.000×10^{0}	0.000×10^{0}	0.000×10^{0}
	0.400×10^{-1}	0.226×10^{-1}	0.250×10^{-1}	0.226×10^{-1}	0.652×10^{-2}	0.138×10^{-1}	0.674×10^{-2}	0.813×10^{-2}	0.934×10^{-2}	0.156×10^{-1}
0.2–0.3	0.234×10^{0}	0.110×10^{0}	0.837×10^{-1}	0.160×10^{-1}	0.178×10^{-1}	0.000×10^{0}	0.778×10^{-2}	0.000×10^{0}	0.000×10^{0}	0.000×10^{0}
	0.337×10^{-1}	0.232×10^{-1}	0.220×10^{-1}	0.935×10^{-2}	0.104×10^{-1}	0.551×10^{-2}	0.793×10^{-2}	0.616×10^{-2}	0.860×10^{-2}	0.427×10^{-2}
0.3–0.4	0.127×10^{0}	0.907×10^{-1}	0.343×10^{-1}	0.328×10^{-1}	0.512×10^{-2}	0.121×10^{-1}	0.000×10^{0}	0.103×10^{-1}	0.873×10^{-2}	0.000×10^{0}
	0.241×10^{-1}	0.192×10^{-1}	0.122×10^{-1}	0.126×10^{-1}	0.516×10^{-2}	0.880×10^{-2}	0.503×10^{-2}	0.111×10^{-1}	0.976×10^{-2}	0.384×10^{-2}
0.4–0.5	0.983×10^{-1}	0.323×10^{-1}	0.273×10^{-1}	0.121×10^{-1}	0.341×10^{-2}	0.390×10^{-2}	0.000×10^{0}	0.000×10^{0}	0.000×10^{0}	0.000×10^{0}
	0.199×10^{-1}	0.108×10^{-1}	0.983×10^{-2}	0.708×10^{-2}	0.344×10^{-2}	0.396×10^{-2}	0.567×10^{-2}	0.423×10^{-2}	0.119×10^{-1}	0.214×10^{-2}
0.5–0.6	0.363×10^{-1}	0.689×10^{-2}	0.132×10^{-1}	0.129×10^{-1}	0.831×10^{-2}	0.000×10^{0}	0.678×10^{-2}	0.000×10^{0}	0.000×10^{0}	0.000×10^{0}
	0.135×10^{-1}	0.691×10^{-2}	0.602×10^{-2}	0.767×10^{-2}	0.609×10^{-2}	0.335×10^{-2}	0.555×10^{-2}	0.688×10^{-2}	0.804×10^{-2}	0.831×10^{-2}
0.6–0.7	0.271×10^{-1}	0.341×10^{-2}	0.420×10^{-2}	0.545×10^{-2}	0.000×10^{0}	0.000×10^{0}	0.000×10^{0}	0.000×10^{0}	0.000×10^{0}	0.000×10^{0}
	0.104×10^{-1}	0.342×10^{-2}	0.425×10^{-2}	0.396×10^{-2}	0.427×10^{-2}	0.759×10^{-2}	0.889×10^{-2}	0.252×10^{-2}	0.168×10^{-2}	0.504×10^{-2}
0.7–0.8	0.466×10^{-2}	0.000×10^{0}	0.240×10^{-2}	0.000×10^{0}	0.000×10^{0}	0.000×10^{0}	0.000×10^{0}	0.000×10^{0}	0.000×10^{0}	0.000×10^{0}
	0.471×10^{-2}	0.464×10^{-2}	0.246×10^{-2}	0.163×10^{-2}	0.232×10^{-1}	0.207×10^{-2}	0.935×10^{-2}	0.224×10^{-2}	0.000×10^{0}	0.168×10^{-2}
0.8–0.9	0.567×10^{-2}	0.000×10^{0}	0.000×10^{0}	0.000×10^{0}	0.000×10^{0}	0.000×10^{0}	0.000×10^{0}	0.000×10^{0}	0.000×10^{0}	0.000×10^{0}
	0.597×10^{-2}	0.248×10^{-1}	0.267×10^{-2}	0.528×10^{-2}	0.393×10^{-2}	0.452×10^{-2}	0.168×10^{-2}	0.000×10^{0}	0.000×10^{0}	0.000×10^{0}
0.9–1.0	0.000×10^{0}	0.000×10^{0}	0.000×10^{0}	0.000×10^{0}	0.000×10^{0}	0.000×10^{0}	0.000×10^{0}	0.000×10^{0}	0.000×10^{0}	0.000×10^{0}
	0.155×10^{-1}	0.904×10^{-2}	0.368×10^{-2}	0.136×10^{-3}	0.000×10^{0}	0.168×10^{-2}	0.000×10^{0}	0.168×10^{-2}	0.000×10^{0}	0.168×10^{-2}
p_T^2 \ Mass	4.0–4.5	4.5–5.0	5.0–5.5	5.5–6.0	6.0–6.5	6.5–7.0	7.0–7.5	7.5–8.0	8.0–8.5	8.5–9.0
0.0–0.5	0.729×10^{-1}	0.382×10^{-1}	0.222×10^{-1}	0.177×10^{-1}	0.139×10^{-2}	0.289×10^{-2}	0.000×10^{0}	0.000×10^{0}	0.000×10^{0}	0.000×10^{0}
	0.959×10^{-2}	0.683×10^{-2}	0.517×10^{-2}	0.483×10^{-2}	0.139×10^{-2}	0.206×10^{-2}	0.139×10^{-2}	0.113×10^{-2}	0.138×10^{-2}	0.114×10^{-2}
0.5–1.0	0.513×10^{-1}	0.255×10^{-1}	0.216×10^{-1}	0.376×10^{-2}	0.433×10^{-2}	0.216×10^{-2}	0.366×10^{-2}	0.000×10^{0}	0.171×10^{-2}	0.000×10^{0}
	0.793×10^{-2}	0.540×10^{-2}	0.536×10^{-2}	0.219×10^{-2}	0.220×10^{-2}	0.155×10^{-2}	0.269×10^{-2}	0.209×10^{-2}	0.183×10^{-2}	0.184×10^{-2}
1.0–1.5	0.318×10^{-1}	0.874×10^{-2}	0.898×10^{-2}	0.226×10^{-2}	0.000×10^{0}	0.000×10^{0}	0.174×10^{-2}	0.240×10^{-2}	0.000×10^{0}	0.000×10^{0}
	0.597×10^{-2}	0.311×10^{-2}	0.322×10^{-2}	0.161×10^{-2}	0.142×10^{-2}	0.124×10^{-2}	0.129×10^{-2}	0.263×10^{-2}	0.200×10^{-2}	0.939×10^{-3}
1.5–2.0	0.172×10^{-1}	0.904×10^{-2}	0.387×10^{-2}	0.471×10^{-2}	0.000×10^{0}	0.000×10^{0}	0.000×10^{0}	0.000×10^{0}	0.000×10^{0}	0.000×10^{0}
	0.438×10^{-2}	0.323×10^{-2}	0.196×10^{-2}	0.240×10^{-2}	0.107×10^{-2}	0.180×10^{-2}	0.199×10^{-2}	0.131×10^{-2}	0.376×10^{-2}	0.594×10^{-3}
2.0–2.5	0.732×10^{-2}	0.204×10^{-2}	0.314×10^{-2}	0.000×10^{0}	0.314×10^{-2}	0.134×10^{-2}	0.000×10^{0}	0.000×10^{0}	0.000×10^{0}	0.000×10^{0}
	0.279×10^{-2}	0.145×10^{-2}	0.183×10^{-2}	0.114×10^{-2}	0.189×10^{-2}	0.138×10^{-2}	0.272×10^{-2}	0.141×10^{-2}	0.200×10^{-2}	0.194×10^{-2}
2.5–3.0	$0.105-10^{-1}$	0.992×10^{-3}	0.220×10^{-2}	0.265×10^{-2}	0.000×10^{0}	0.117×10^{-2}	0.000×10^{0}	0.000×10^{0}	0.000×10^{0}	0.000×10^{0}
	0.323×10^{-2}	0.995×10^{-3}	0.158×10^{-2}	0.158×10^{-2}	0.100×10^{-2}	0.122×10^{-2}	0.157×10^{-2}	0.172×10^{-2}	0.168×10^{-2}	0.100×10^{-2}
3.0–3.5	0.844×10^{-2}	0.484×10^{-2}	0.130×10^{-2}	0.187×10^{-2}	0.000×10^{0}	0.000×10^{0}	0.000×10^{0}	0.000×10^{0}	0.000×10^{0}	0.000×10^{0}
	0.326×10^{-2}	0.221×10^{-2}	0.132×10^{-2}	0.192×10^{-2}	0.158×10^{-2}	0.201×10^{-2}	0.583×10^{-3}	0.299×10^{-2}	0.300×10^{-2}	0.165×10^{-2}

TABLE III. (*Continued*).

$\bar{p}$

p_T^2 \ Mass	4.0–4.5	4.5–5.0	5.0–5.5	5.5–6.0	6.0–6.5	6.5–7.0	7.0–7.5	7.5–8.0	8.0–8.5	8.5–9.0
3.5–4.0	0.330×10^{-2}	0.177×10^{-2}	0.116×10^{-2}	0.000×10^{0}	0.000×10^{0}	0.000×10^{0}	0.000×10^{0}	0.000×10^{0}	0.000×10^{0}	0.000×10^{0}
	0.193×10^{-2}	0.126×10^{-2}	0.118×10^{-2}	0.852×10^{-3}	0.122×10^{-2}	0.115×10^{-2}	0.132×10^{-2}	0.660×10^{-3}	0.336×10^{-3}	0.000×10^{0}
4.0–4.5	0.104×10^{-2}	0.125×10^{-2}	0.000×10^{0}	0.805×10^{-3}	0.580×10^{-3}	0.000×10^{0}	0.000×10^{0}	0.000×10^{0}	0.000×10^{0}	0.000×10^{0}
	0.105×10^{-2}	0.126×10^{-2}	0.715×10^{-3}	0.829×10^{-3}	0.621×10^{-3}	0.222×10^{-2}	0.628×10^{-3}	0.163×10^{-2}	0.165×10^{-2}	0.000×10^{0}
4.5–5.0	0.717×10^{-3}	0.000×10^{0}	0.669×10^{-3}	0.788×10^{-3}	0.000×10^{0}	0.000×10^{0}	0.000×10^{0}	0.000×10^{0}	0.000×10^{0}	0.000×10^{0}
	0.722×10^{-3}	0.886×10^{-3}	0.686×10^{-3}	0.821×10^{-3}	0.200×10^{-2}	0.133×10^{-2}	0.267×10^{-2}	0.187×10^{-3}	0.336×10^{-3}	0.000×10^{0}
5.0–5.5	0.764×10^{-3}	0.000×10^{0}	0.000×10^{0}	0.000×10^{0}	0.000×10^{0}	0.000×10^{0}	0.00×10^{0}	0.000×10^{0}	0.000×10^{0}	0.000×10^{0}
	0.771×10^{-3}	0.717×10^{-3}	0.102×10^{-2}	0.201×10^{-2}	0.105×10^{-2}	0.430×10^{-2}	0.198×10^{-2}	0.336×10^{-3}	0.000×10^{0}	0.664×10^{-3}
5.5–6.0	0.207×10^{-2}	0.000×10^{0}	0.000×10^{0}	0.000×10^{0}	0.000×10^{0}	0.000×10^{0}	0.000×10^{0}	0.000×10^{0}	0.000×10^{0}	0.000×10^{0}
	0.152×10^{-2}	0.116×10^{-2}	0.105×10^{-2}	0.121×10^{-2}	0.190×10^{-3}	0.161×10^{-2}	0.991×10^{-3}	0.336×10^{-3}	0.000×10^{0}	0.000×10^{0}
6.0–6.5	0.262×10^{-2}	0.000×10^{0}	0.000×10^{0}	0.000×10^{0}	0.000×10^{0}	0.000×10^{0}	0.000×10^{0}	0.000×10^{0}	0.000×10^{0}	0.000×10^{0}
	0.197×10^{-2}	0.781×10^{-3}	0.142×10^{-2}	0.628×10^{-3}	0.480×10^{-3}	0.141×10^{-2}	0.318×10^{-3}	0.336×10^{-3}	0.986×10^{-3}	0.000×10^{0}
6.5–7.0	0.000×10^{0}	0.000×10^{0}	0.000×10^{0}	0.000×10^{0}	0.000×10^{0}	0.000×10^{0}	0.000×10^{0}	0.000×10^{0}	0.000×10^{0}	0.000×10^{0}
	0.781×10^{-3}	0.279×10^{-2}	0.124×10^{-2}	0.194×10^{-2}	0.805×10^{-3}	0.586×10^{-3}	0.599×10^{-3}	0.000×10^{0}	0.000×10^{0}	0.000×10^{0}
7.0–7.5	0.000×10^{0}	0.000×10^{0}	0.000×10^{0}	0.000×10^{0}	0.000×10^{0}	0.000×10^{0}	0.000×10^{0}	0.000×10^{0}	0.000×10^{0}	0.000×10^{0}
	0.771×10^{-3}	0.684×10^{-3}	0.911×10^{-3}	0.333×10^{-2}	0.131×10^{-2}	0.132×10^{-2}	0.248×10^{-3}	0.000×10^{0}	0.000×10^{0}	0.000×10^{0}

p_T^2 \ x_F	−0.10–0.0	0.0–0.10	0.10–0.20	0.20–0.30	0.30–0.40	0.40–0.50	0.50–0.60	0.60–0.70	0.70–0.80	0.80–0.90	0.90–1.0
0.0–0.5	0.222×10^{0}	0.210×10^{0}	0.152×10^{0}	0.210×10^{0}	0.973×10^{-1}	0.756×10^{-1}	0.216×10^{-1}	0.131×10^{-1}	0.394×10^{-2}	0.000×10^{0}	0.000×10^{0}
	0.648×10^{-1}	0.476×10^{-1}	0.327×10^{-1}	0.343×10^{-1}	0.222×10^{-1}	0.176×10^{-1}	0.102×10^{-1}	0.770×10^{-2}	0.399×10^{-2}	0.581×10^{-2}	0.478×10^{-2}
0.5–1.0	0.134×10^{0}	0.148×10^{0}	0.133×10^{0}	0.109×10^{0}	0.949×10^{-1}	0.283×10^{-1}	0.320×10^{-1}	0.134×10^{-1}	0.000×10^{0}	0.925×10^{-2}	0.000×10^{0}
	0.480×10^{-1}	0.401×10^{-1}	0.318×10^{-1}	0.242×10^{-1}	0.201×10^{-1}	0.101×10^{-1}	0.129×10^{-1}	0.685×10^{-2}	0.367×10^{-2}	0.101×10^{-1}	0.527×10^{-2}
1.0–1.5	0.124×10^{0}	0.718×10^{-1}	0.769×10^{-1}	0.568×10^{-1}	0.395×10^{-1}	0.286×10^{-1}	0.678×10^{-2}	0.000×10^{0}	0.336×10^{-2}	0.000×10^{0}	0.000×10^{0}
	0.449×10^{-1}	0.274×10^{-1}	0.225×10^{-1}	0.166×10^{-1}	0.126×10^{-1}	0.114×10^{-1}	0.483×10^{-2}	0.400×10^{-2}	0.347×10^{-2}	0.354×10^{-2}	0.508×10^{-2}
1.5–2.0	0.381×10^{-1}	0.436×10^{-1}	0.320×10^{-1}	0.274×10^{-1}	0.286×10^{-1}	0.205×10^{-1}	0.986×10^{-2}	0.447×10^{-2}	0.000×10^{0}	0.000×10^{0}	0.000×10^{0}
	0.272×10^{-1}	0.220×10^{-1}	0.144×10^{-1}	0.113×10^{-1}	0.118×10^{-1}	0.794×10^{-2}	0.580×10^{-2}	0.455×10^{-2}	0.708×10^{-2}	0.354×10^{-2}	0.171×10^{-2}
2.0–2.5	0.366×10^{-1}	0.251×10^{-1}	0.231×10^{-1}	0.142×10^{-1}	0.876×10^{-2}	0.724×10^{-2}	0.440×10^{-2}	0.349×10^{-2}	0.000×10^{0}	0.000×10^{0}	0.000×10^{0}
	0.262×10^{-1}	0.146×10^{-1}	0.116×10^{-1}	0.826×10^{-2}	0.623×10^{-2}	0.517×10^{-2}	0.445×10^{-2}	0.357×10^{-2}	0.403×10^{-2}	0.155×10^{-1}	0.168×10^{-2}
2.5–3.0	0.488×10^{-1}	0.252×10^{-1}	0.135×10^{-1}	0.252×10^{-1}	0.972×10^{-2}	0.129×10^{-1}	0.000×10^{0}	0.200×10^{-2}	0.000×10^{0}	0.000×10^{0}	0.000×10^{0}
	0.289×10^{-1}	0.148×10^{-1}	0.964×10^{-2}	0.105×10^{-1}	0.569×10^{-2}	0.768×10^{-2}	0.286×10^{-2}	0.205×10^{-2}	0.354×10^{-2}	0.683×10^{-2}	0.000×10^{0}
3.0–3.5	0.000×10^{0}	0.329×10^{-1}	0.150×10^{-1}	0.927×10^{-2}	0.271×10^{-1}	0.391×10^{-2}	0.000×10^{0}	0.000×10^{0}	0.000×10^{0}	0.000×10^{0}	0.000×10^{0}
	0.206×10^{-1}	0.194×10^{-1}	0.107×10^{-1}	0.662×10^{-2}	0.115×10^{-1}	0.396×10^{-2}	0.416×10^{-2}	0.545×10^{-2}	0.124×10^{-1}	0.302×10^{-2}	0.000×10^{0}
3.5–4.0	0.234×10^{-1}	0.000×10^{0}	0.000×10^{0}	0.106×10^{-1}	0.370×10^{-2}	0.000×10^{0}	0.922×10^{-2}	0.000×10^{0}	0.000×10^{0}	0.000×10^{0}	0.000×10^{0}
	0.170×10^{-1}	0.115×10^{-1}	0.643×10^{-2}	0.624×10^{-2}	0.375×10^{-2}	0.362×10^{-2}	0.704×10^{-2}	0.176×10^{-2}	0.370×10^{-2}	0.400×10^{-2}	0.168×10^{-2}
4.0–4.5	0.000×10^{0}	0.000×10^{0}	0.124×10^{-1}	0.417×10^{-2}	0.371×10^{-2}	0.000×10^{0}	0.000×10^{0}	0.000×10^{0}	0.000×10^{0}	0.000×10^{0}	0.000×10^{0}
	0.230×10^{-1}	0.848×10^{-2}	0.906×10^{-2}	0.422×10^{-2}	0.377×10^{-2}	0.371×10^{-2}	0.438×10^{-2}	0.305×10^{-2}	0.586×10^{-2}	0.168×10^{-2}	0.168×10^{-2}
4.5–5.0	0.971×10^{-2}	0.000×10^{0}	0.971×10^{-2}	0.000×10^{0}	0.000×10^{0}	0.000×10^{0}	0.000×10^{0}	0.578×10^{-2}	0.000×10^{0}	0.000×10^{0}	0.000×10^{0}
	0.997×10^{-2}	0.745×10^{-2}	0.706×10^{-2}	0.328×10^{-2}	0.292×10^{-2}	0.202×10^{-2}	0.337×10^{-2}	0.708×10^{-2}	0.319×10^{-2}	0.168×10^{-2}	0.168×10^{-2}
5.0–5.5	0.000×10^{0}	0.000×10^{0}	0.000×10^{0}	0.593×10^{-2}	0.000×10^{0}	0.000×10^{0}	0.000×10^{0}	0.000×10^{0}	0.000×10^{0}	0.000×10^{0}	0.000×10^{0}
	0.155×10^{-1}	0.752×10^{-2}	0.359×10^{-2}	0.611×10^{-2}	0.282×10^{-2}	0.304×10^{-2}	0.336×10^{-2}	0.100×10^{-1}	0.294×10^{-2}	0.000×10^{0}	0.000×10^{0}

TABLE III. (*Continued*).

$\bar{p}$

p_T^2 \ x_F	−0.10–0.0	0.0–0.10	0.10–0.20	0.20–0.30	0.30–0.40	0.40–0.50	0.50–0.60	0.60–0.70	0.70–0.80	0.80–0.90	0.90–1.0
5.5–6.0	0.166×10^{-1}	0.000×10^{0}	0.586×10^{-2}	0.000×10^{0}	0.000×10^{0}	0.257×10^{-2}	0.000×10^{0}	0.000×10^{0}	0.000×10^{0}	0.000×10^{0}	0.000×10^{0}
	0.180×10^{-1}	0.770×10^{-2}	0.608×10^{-2}	0.438×10^{-2}	0.714×10^{-2}	0.275×10^{-2}	0.501×10^{-2}	0.974×10^{-3}	0.168×10^{-2}	0.000×10^{0}	0.000×10^{0}
6.0–6.5	0.000×10^{0}	0.000×10^{0}	0.489×10^{-2}	0.331×10^{-2}	0.000×10^{0}	0.000×10^{0}	0.000×10^{0}	0.000×10^{0}	0.000×10^{0}	0.000×10^{0}	0.000×10^{0}
	0.161×10^{-1}	0.171×10^{-1}	0.505×10^{-2}	0.346×10^{-2}	0.360×10^{-2}	0.542×10^{-2}	0.487×10^{-2}	0.104×10^{-2}	0.000×10^{0}	0.000×10^{0}	0.168×10^{-2}
6.5–7.0	0.000×10^{0}	0.000×10^{0}	0.000×10^{0}	0.000×10^{0}	0.000×10^{0}	0.000×10^{0}	0.000×10^{0}	0.000×10^{0}	0.000×10^{0}	0.000×10^{0}	0.000×10^{0}
	0.972×10^{-2}	0.717×10^{-2}	0.138×10^{-1}	0.340×10^{-2}	0.242×10^{-2}	0.657×10^{-2}	0.336×10^{-2}	0.145×10^{-2}	0.319×10^{-2}	0.000×10^{0}	0.000×10^{0}
7.0–7.5	0.000×10^{0}	0.000×10^{0}	0.302×10^{-2}	0.000×10^{0}	0.000×10^{0}	0.000×10^{0}	0.000×10^{0}	0.000×10^{0}	0.000×10^{0}	0.000×10^{0}	0.000×10^{0}
	0.148×10^{-1}	0.198×10^{-1}	0.320×10^{-2}	0.109×10^{-1}	0.325×10^{-2}	0.127×10^{-2}	0.502×10^{-2}	0.478×10^{-2}	0.168×10^{-2}	0.168×10^{-2}	0.000×10^{0}

π^-

x_F \ Mass	4.0–4.5	4.5–5.0	5.0–5.5	5.5–6.0	6.0–6.5	6.5–7.0	7.0–7.5	7.5–8.0	8.0–8.5	8.5–9.0
−0.1–0.0	0.173×10^{0}	0.952×10^{-1}	0.158×10^{-1}	0.185×10^{-1}	0.110×10^{-1}	0.000×10^{0}	0.873×10^{-2}	0.510×10^{-2}	0.000×10^{0}	0.000×10^{0}
	0.352×10^{-1}	0.254×10^{-1}	0.922×10^{-2}	0.945×10^{-2}	0.794×10^{-2}	0.520×10^{-2}	0.641×10^{-2}	0.527×10^{-2}	0.679×10^{-2}	0.178×10^{-1}
0.0–0.1	0.146×10^{0}	0.638×10^{-1}	0.424×10^{-1}	0.242×10^{-1}	0.100×10^{-1}	0.129×10^{-1}	0.000×10^{0}	0.000×10^{0}	0.303×10^{-2}	0.000×10^{0}
	0.234×10^{-1}	0.153×10^{-1}	0.130×10^{-1}	0.100×10^{-1}	0.590×10^{-2}	0.768×10^{-2}	0.308×10^{-2}	0.418×10^{-2}	0.312×10^{-2}	0.414×10^{-1}
0.1–0.2	0.165×10^{0}	0.657×10^{-1}	0.592×10^{-1}	0.226×10^{-1}	0.235×10^{-1}	0.786×10^{-2}	0.967×10^{-2}	0.262×10^{-2}	0.375×10^{-2}	0.208×10^{-2}
	0.207×10^{-1}	0.124×10^{-1}	0.126×10^{-1}	0.811×10^{-2}	0.854×10^{-2}	0.564×10^{-2}	0.576×10^{-2}	0.266×10^{-2}	0.388×10^{-2}	0.217×10^{-2}
0.2–0.3	0.169×10^{0}	0.882×10^{-1}	0.422×10^{-1}	0.162×10^{-1}	0.143×10^{-1}	0.113×10^{-1}	0.769×10^{-2}	0.482×10^{-2}	0.260×10^{-2}	0.000×10^{0}
	0.178×10^{-1}	0.133×10^{-1}	0.980×10^{-2}	0.582×10^{-2}	0.550×10^{-2}	0.520×10^{-2}	0.456×10^{-2}	0.350×10^{-2}	0.266×10^{-2}	0.328×10^{-2}
0.3–0.4	0.138×10^{0}	0.529×10^{-1}	0.327×10^{-1}	0.234×10^{-1}	0.170×10^{-1}	0.374×10^{-2}	0.816×10^{-2}	0.730×10^{-2}	0.000×10^{0}	0.202×10^{-2}
	0.150×10^{-1}	0.872×10^{-2}	0.743×10^{-2}	0.615×10^{-2}	0.580×10^{-2}	0.266×10^{-2}	0.419×10^{-2}	0.439×10^{-2}	0.224×10^{-2}	0.208×10^{-2}
0.4–0.5	0.104×10^{0}	0.707×10^{-1}	0.374×10^{-1}	0.239×10^{-1}	0.129×10^{-1}	0.638×10^{-2}	0.514×10^{-2}	0.000×10^{0}	0.000×10^{0}	0.000×10^{0}
	0.132×10^{-1}	0.102×10^{-1}	0.736×10^{-2}	0.610×10^{-2}	0.439×10^{-2}	0.324×10^{-2}	0.304×10^{-2}	0.169×10^{-2}	0.148×10^{-2}	0.212×10^{-2}
0.5–0.6	0.941×10^{-1}	0.471×10^{-1}	0.267×10^{-1}	0.167×10^{-1}	0.105×10^{-1}	0.886×10^{-2}	0.113×10^{-1}	0.469×10^{-2}	0.000×10^{0}	0.000×10^{0}
	0.130×10^{-1}	0.860×10^{-2}	0.610×10^{-2}	0.474×10^{-2}	0.381×10^{-2}	0.345×10^{-2}	0.491×10^{-2}	0.282×10^{-2}	0.191×10^{-2}	0.959×10^{-3}
0.6–0.7	0.703×10^{-1}	0.413×10^{-1}	0.227×10^{-1}	0.156×10^{-1}	0.110×10^{-1}	0.429×10^{-2}	0.000×10^{0}	0.511×10^{-2}	0.000×10^{0}	0.000×10^{0}
	0.129×10^{-1}	0.878×10^{-2}	0.600×10^{-2}	0.469×10^{-2}	0.449×10^{-2}	0.219×10^{-2}	0.118×10^{-2}	0.313×10^{-2}	0.141×10^{-2}	0.237×10^{-2}
0.7–0.8	0.536×10^{-1}	0.237×10^{-1}	0.153×10^{-1}	0.484×10^{-2}	0.486×10^{-2}	0.101×10^{-1}	0.144×10^{-2}	0.184×10^{-2}	0.000×10^{0}	0.177×10^{-2}
	0.138×10^{-1}	0.768×10^{-2}	0.591×10^{-2}	0.283×10^{-2}	0.286×10^{-2}	0.436×10^{-2}	0.146×10^{-2}	0.190×10^{-2}	0.470×10^{-2}	0.194×10^{-2}
0.8–0.9	0.200×10^{-1}	0.153×10^{-1}	0.542×10^{-2}	0.524×10^{-2}	0.000×10^{0}	0.145×10^{-2}	0.000×10^{0}	0.204×10^{-2}	0.321×10^{-2}	0.000×10^{0}
	0.118×10^{-1}	0.784×10^{-2}	0.389×10^{-2}	0.379×10^{-2}	0.359×10^{-2}	0.147×10^{-2}	0.176×10^{-2}	0.219×10^{-2}	0.371×10^{-2}	0.842×10^{-2}
0.9–1.0	0.000×10^{0}	0.000×10^{0}	0.443×10^{-2}	0.000×10^{0}	0.000×10^{0}	0.309×10^{-2}	0.000×10^{0}	0.000×10^{0}	0.000×10^{0}	0.000×10^{0}
	0.130×10^{-1}	0.125×10^{-1}	0.468×10^{-2}	0.487×10^{-2}	0.308×10^{-2}	0.363×10^{-2}	0.706×10^{-2}	0.259×10^{-2}	0.111×10^{-2}	0.161×10^{-3}

p_T^2 \ Mass	4.0–4.5	4.5–5.0	5.0–5.5	5.5–6.0	6.0–6.5	6.5–7.0	7.0–7.5	7.5–8.0	8.0–8.5	8.5–9.0
0.0–0.5	0.625×10^{-1}	0.351×10^{-1}	0.214×10^{-1}	0.671×10^{-2}	0.675×10^{-2}	0.338×10^{-2}	0.286×10^{-2}	0.300×10^{-2}	0.130×10^{-2}	0.486×10^{-3}
	0.527×10^{-2}	0.382×10^{-2}	0.300×10^{-2}	0.164×10^{-2}	0.176×10^{-2}	0.121×10^{-2}	0.119×10^{-2}	0.127×10^{-2}	0.776×10^{-3}	0.496×10^{-3}
0.5–1.0	0.436×10^{-1}	0.205×10^{-1}	0.144×10^{-1}	0.756×10^{-2}	0.432×10^{-2}	0.376×10^{-2}	0.123×10^{-2}	0.991×10^{-3}	0.000×10^{0}	0.000×10^{0}
	0.440×10^{-2}	0.287×10^{-2}	0.250×10^{-2}	0.177×10^{-2}	0.132×10^{-2}	0.122×10^{-2}	0.727×10^{-3}	0.714×10^{-3}	0.560×10^{-3}	0.785×10^{-3}

TABLE III. (*Continued*).

π^-

p_T^2 \ Mass	4.0–4.5	4.5–5.0	5.0–5.5	5.5–6.0	6.0–6.5	6.5–7.0	7.0–7.5	7.5–8.0	8.0–8.5	8.5–9.0
1.0–1.5	0.317×10^{-1}	0.133×10^{-1}	0.523×10^{-2}	0.465×10^{-2}	0.425×10^{-2}	0.295×10^{-2}	0.179×10^{-2}	0.890×10^{-3}	0.000×10^{0}	0.508×10^{-3}
	0.379×10^{-2}	0.230×10^{-2}	0.141×10^{-2}	0.131×10^{-2}	0.138×10^{-2}	0.136×10^{-2}	0.928×10^{-3}	0.647×10^{-3}	0.716×10^{-3}	0.527×10^{-3}
1.5–2.0	0.203×10^{-1}	0.856×10^{-2}	0.417×10^{-2}	0.467×10^{-2}	0.198×10^{-2}	0.159×10^{-2}	0.740×10^{-3}	0.747×10^{-3}	0.396×10^{-3}	0.000×10^{0}
	0.299×10^{-2}	0.178×10^{-2}	0.127×10^{-2}	0.128×10^{-2}	0.827×10^{-3}	0.734×10^{-3}	0.534×10^{-3}	0.548×10^{-3}	0.409×10^{-3}	0.202×10^{-3}
2.0–2.5	0.126×10^{-1}	0.489×10^{-2}	0.330×10^{-2}	0.518×10^{-2}	0.132×10^{-2}	0.338×10^{-3}	0.727×10^{-3}	0.000×10^{0}	0.000×10^{0}	0.362×10^{-3}
	0.236×10^{-2}	0.138×10^{-2}	0.118×10^{-2}	0.156×10^{-2}	0.777×10^{-3}	0.341×10^{-3}	0.529×10^{-3}	0.396×10^{-3}	0.446×10^{-3}	0.384×10^{-3}
2.5–3.0	0.595×10^{-2}	0.368×10^{-2}	0.247×10^{-2}	0.786×10^{-3}	0.430×10^{-3}	0.498×10^{-3}	0.605×10^{-3}	0.594×10^{-3}	0.000×10^{0}	0.000×10^{0}
	0.156×10^{-2}	0.113×10^{-2}	0.102×10^{-2}	0.562×10^{-3}	0.434×10^{-3}	0.509×10^{-3}	0.445×10^{-3}	0.576×10^{-3}	0.332×10^{-3}	0.104×10^{-2}
3.0–3.5	0.356×10^{-2}	0.199×10^{-2}	0.195×10^{-2}	0.176×10^{-2}	0.000×10^{0}	0.988×10^{-3}	0.000×10^{0}	0.216×10^{-3}	0.000×10^{0}	0.000×10^{0}
	0.133×10^{-2}	0.106×10^{-2}	0.816×10^{-3}	0.815×10^{-3}	0.278×10^{-3}	0.602×10^{-3}	0.536×10^{-3}	0.225×10^{-3}	0.718×10^{-3}	0.432×10^{-3}
3.5–4.0	0.328×10^{-2}	0.166×10^{-2}	0.113×10^{-2}	0.000×10^{0}	0.152×10^{-2}	0.000×10^{0}	0.000×10^{0}	0.000×10^{0}	0.000×10^{0}	0.000×10^{0}
	0.118×10^{-2}	0.894×10^{-3}	0.669×10^{-3}	0.382×10^{-3}	0.941×10^{-3}	0.640×10^{-3}	0.509×10^{-3}	0.420×10^{-3}	0.377×10^{-3}	0.174×10^{-2}
4.0–4.5	0.335×10^{-2}	0.123×10^{-2}	0.874×10^{-3}	0.000×10^{0}	0.390×10^{-3}	0.337×10^{-3}	0.636×10^{-3}	0.000×10^{0}	0.000×10^{0}	0.000×10^{0}
	0.121×10^{-2}	0.631×10^{-3}	0.516×10^{-3}	0.428×10^{-3}	0.400×10^{-3}	0.348×10^{-3}	0.697×10^{-3}	0.426×10^{-3}	0.165×10^{-3}	0.377×10^{-3}
4.5–5.0	0.234×10^{-2}	0.214×10^{-2}	0.405×10^{-3}	0.000×10^{0}	0.278×10^{-3}	0.000×10^{0}	0.000×10^{0}	0.000×10^{0}	0.000×10^{0}	0.000×10^{0}
	0.985×10^{-3}	0.100×10^{-2}	0.410×10^{-3}	0.269×10^{-3}	0.286×10^{-3}	0.215×10^{-3}	0.423×10^{-3}	0.480×10^{-3}	0.316×10^{-3}	0.126×10^{-3}
5.0–5.5	0.620×10^{-3}	0.315×10^{-3}	0.108×10^{-2}	0.000×10^{0}	0.000×10^{0}	0.000×10^{0}	0.000×10^{0}	0.000×10^{0}	0.000×10^{0}	0.000×10^{0}
	0.444×10^{-3}	0.318×10^{-3}	0.660×10^{-3}	0.310×10^{-3}	0.253×10^{-3}	0.322×10^{-3}	0.253×10^{-3}	0.488×10^{-3}	0.377×10^{-3}	0.539×10^{-3}
5.5–6.0	0.100×10^{-2}	0.113×10^{-2}	0.721×10^{-3}	0.000×10^{0}	0.779×10^{-3}	0.000×10^{0}	0.000×10^{0}	0.000×10^{0}	0.000×10^{0}	0.000×10^{0}
	0.727×10^{-3}	0.690×10^{-3}	0.536×10^{-3}	0.342×10^{-3}	0.618×10^{-3}	0.281×10^{-3}	0.387×10^{-3}	0.742×10^{-3}	0.628×10^{-3}	0.252×10^{-3}
6.0–6.5	0.129×10^{-2}	0.702×10^{-3}	0.000×10^{0}	0.000×10^{0}	0.000×10^{0}	0.265×10^{-3}	0.000×10^{0}	0.000×10^{0}	0.000×10^{0}	0.000×10^{0}
	0.680×10^{-3}	0.514×10^{-3}	0.285×10^{-3}	0.294×10^{-3}	0.921×10^{-3}	0.307×10^{-3}	0.153×10^{-3}	0.457×10^{-3}	0.230×10^{-3}	0.000×10^{0}
6.5–7.0	0.249×10^{-3}	0.200×10^{-3}	0.000×10^{0}	0.000×10^{0}	0.000×10^{0}	0.000×10^{0}	0.000×10^{0}	0.000×10^{0}	0.000×10^{0}	0.000×10^{0}
	0.253×10^{-3}	0.204×10^{-3}	0.468×10^{-3}	0.621×10^{-3}	0.579×10^{-3}	0.988×10^{-3}	0.739×10^{-3}	0.499×10^{-3}	0.000×10^{0}	0.000×10^{0}
7.0–7.5	0.000×10^{0}	0.000×10^{0}	0.000×10^{0}	0.000×10^{0}	0.000×10^{0}	0.000×10^{0}	0.000×10^{0}	0.000×10^{0}	0.000×10^{0}	0.000×10^{0}
	0.287×10^{-3}	0.416×10^{-3}	0.261×10^{-3}	0.282×10^{-3}	0.440×10^{-3}	0.319×10^{-3}	0.144×10^{-3}	0.378×10^{-3}	0.249×10^{-3}	0.126×10^{-3}

p_T^2 \ x_F	−0.1–0.0	0.0–0.1	0.1–0.2	0.2–0.3	0.3–0.4	0.4–0.5	0.5–0.6	0.6–0.7	0.7–0.8	0.8–0.9	0.9–1.0
0.0–0.5	0.122×10^{0}	0.134×10^{0}	0.113×10^{0}	0.120×10^{0}	0.794×10^{-1}	0.860×10^{-1}	0.607×10^{-1}	0.661×10^{-1}	0.481×10^{-1}	0.212×10^{-1}	0.103×10^{-1}
	0.289×10^{-1}	0.230×10^{-1}	0.175×10^{-1}	0.156×10^{-1}	0.114×10^{-1}	0.118×10^{-1}	0.101×10^{-1}	0.116×10^{-1}	0.113×10^{-1}	0.970×10^{-2}	0.765×10^{-2}
0.5–1.0	0.623×10^{-1}	0.787×10^{-1}	0.756×10^{-1}	0.776×10^{-1}	0.703×10^{-1}	0.617×10^{-1}	0.490×10^{-1}	0.297×10^{-1}	0.258×10^{-1}	0.153×10^{-1}	0.000×10^{0}
	0.192×10^{-1}	0.176×10^{-1}	0.148×10^{-1}	0.127×10^{-1}	0.110×10^{-1}	0.984×10^{-2}	0.863×10^{-2}	0.736×10^{-2}	0.801×10^{-2}	0.790×10^{-2}	0.673×10^{-2}
1.0–1.5	0.507×10^{-1}	0.242×10^{-1}	0.489×10^{-1}	0.474×10^{-1}	0.570×10^{-1}	0.431×10^{-1}	0.376×10^{-1}	0.216×10^{-1}	0.126×10^{-1}	0.789×10^{-2}	0.731×10^{-2}
	0.174×10^{-1}	0.926×10^{-2}	0.114×10^{-1}	0.102×10^{-1}	0.976×10^{-2}	0.807×10^{-2}	0.789×10^{-2}	0.637×10^{-2}	0.578×10^{-2}	0.570×10^{-2}	0.772×10^{-2}
1.5–2.0	0.195×10^{-1}	0.212×10^{-1}	0.361×10^{-1}	0.307×10^{-1}	0.210×10^{-1}	0.190×10^{-1}	0.275×10^{-1}	0.303×10^{-1}	0.171×10^{-1}	0.725×10^{-2}	0.000×10^{0}
	0.114×10^{-1}	0.880×10^{-2}	0.956×10^{-2}	0.739×10^{-2}	0.572×10^{-2}	0.535×10^{-2}	0.668×10^{-2}	0.709×10^{-2}	0.630×10^{-2}	0.528×10^{-2}	0.266×10^{-1}
2.0–2.5	0.127×10^{-1}	0.146×10^{-1}	0.289×10^{-1}	0.283×10^{-1}	0.182×10^{-1}	0.189×10^{-1}	0.133×10^{-1}	0.106×10^{-1}	0.219×10^{-2}	0.312×10^{-2}	0.000×10^{0}
	0.914×10^{-2}	0.745×10^{-2}	0.861×10^{-2}	0.752×10^{-2}	0.559×10^{-2}	0.574×10^{-2}	0.456×10^{-2}	0.444×10^{-2}	0.221×10^{-2}	0.319×10^{-2}	0.561×10^{-2}
2.5–3.0	0.163×10^{-1}	0.108×10^{-1}	0.128×10^{-1}	0.206×10^{-1}	0.133×10^{-1}	0.808×10^{-2}	0.471×10^{-2}	0.000×10^{0}	0.238×10^{-2}	0.000×10^{0}	0.000×10^{0}
	0.974×10^{-2}	0.638×10^{-2}	0.535×10^{-2}	0.641×10^{-2}	0.455×10^{-2}	0.335×10^{-2}	0.275×10^{-2}	0.183×10^{-2}	0.241×10^{-2}	0.420×10^{-2}	0.244×10^{-1}

TABLE III. (*Continued*).

π^-

p_T^2 \ x_F	−0.1–0.0	0.0–0.1	0.1–0.2	0.2–0.3	0.3–0.4	0.4–0.5	0.5–0.6	0.6–0.7	0.7–0.8	0.8–0.9	0.9–1.0
3.0–3.5	0.000×10^{0}	0.336×10^{-2}	0.148×10^{-1}	0.856×10^{-2}	0.433×10^{-2}	0.667×10^{-2}	0.808×10^{-2}	0.317×10^{-2}	0.255×10^{-2}	0.000×10^{0}	0.000×10^{0}
	0.598×10^{-2}	0.339×10^{-2}	0.579×10^{-2}	0.436×10^{-2}	0.252×10^{-2}	0.358×10^{-2}	0.339×10^{-2}	0.319×10^{-2}	0.260×10^{-2}	0.437×10^{-2}	0.900×10^{-2}
3.5–4.0	0.000×10^{0}	0.369×10^{-2}	0.104×10^{-1}	0.656×10^{-2}	0.604×10^{-2}	0.327×10^{-2}	0.458×10^{-2}	0.171×10^{-2}	0.000×10^{0}	0.000×10^{0}	-0.784×10^{-2}
	0.593×10^{-2}	0.374×10^{-2}	0.480×10^{-2}	0.335×10^{-2}	0.308×10^{-2}	0.234×10^{-2}	0.270×10^{-2}	0.173×10^{-2}	0.338×10^{-2}	0.471×10^{-2}	0.111×10^{-1}
4.0–4.5	0.496×10^{-2}	0.155×10^{-1}	0.241×10^{-2}	0.152×10^{-2}	0.326×10^{-2}	0.427×10^{-2}	0.379×10^{-2}	0.616×10^{-2}	0.221×10^{-2}	0.000×10^{0}	0.000×10^{0}
	0.507×10^{-2}	0.957×10^{-2}	0.243×10^{-2}	0.153×10^{-2}	0.191×10^{-2}	0.252×10^{-2}	0.226×10^{-2}	0.378×10^{-2}	0.228×10^{-2}	0.202×10^{-2}	0.531×10^{-2}
4.5–5.0	0.835×10^{-2}	0.000×10^{0}	0.361×10^{-2}	0.411×10^{-2}	0.437×10^{-2}	0.316×10^{-2}	0.478×10^{-2}	0.000×10^{0}	0.000×10^{0}	0.000×10^{0}	0.000×10^{0}
	0.882×10^{-2}	0.436×10^{-2}	0.261×10^{-2}	0.297×10^{-2}	0.260×10^{-2}	0.187×10^{-2}	0.288×10^{-2}	0.186×10^{-2}	0.249×10^{-2}	0.110×10^{-1}	0.469×10^{-2}
5.0–5.5	0.125×10^{-1}	0.000×10^{0}	0.218×10^{-2}	0.192×10^{-2}	0.000×10^{0}	0.297×10^{-2}	0.897×10^{-3}	0.000×10^{0}	0.000×10^{0}	0.000×10^{0}	0.000×10^{0}
	0.100×10^{-1}	0.300×10^{-2}	0.222×10^{-2}	0.196×10^{-2}	0.112×10^{-2}	0.177×10^{-2}	0.891×10^{-3}	0.201×10^{-2}	0.485×10^{-2}	0.314×10^{-2}	0.688×10^{-2}
5.5–6.0	0.000×10^{0}	0.000×10^{0}	0.665×10^{-2}	0.756×10^{-2}	0.000×10^{0}	0.173×10^{-2}	0.148×10^{-2}	0.000×10^{0}	0.000×10^{0}	0.000×10^{0}	0.000×10^{0}
	0.517×10^{-2}	0.218×10^{-2}	0.503×10^{-2}	0.369×10^{-2}	0.215×10^{-2}	0.178×10^{-2}	0.153×10^{-2}	0.153×10^{-2}	0.732×10^{-2}	0.113×10^{-1}	0.156×10^{-2}
6.0–6.5	0.374×10^{-2}	0.393×10^{-2}	0.179×10^{-2}	0.125×10^{-2}	0.196×10^{-2}	0.000×10^{0}	0.183×10^{-2}	0.000×10^{0}	0.189×10^{-2}	0.000×10^{0}	0.000×10^{0}
	0.400×10^{-2}	0.421×10^{-2}	0.185×10^{-2}	0.128×10^{-2}	0.142×10^{-2}	0.115×10^{-2}	0.194×10^{-2}	0.153×10^{-2}	0.207×10^{-2}	0.672×10^{-2}	0.279×10^{-2}
6.5–7.0	0.310×10^{-2}	0.000×10^{0}	0.000×10^{0}	0.000×10^{0}	0.125×10^{-2}	0.880×10^{-3}	0.000×10^{0}	0.000×10^{0}	0.000×10^{0}	0.000×10^{0}	0.000×10^{0}
	0.335×10^{-2}	0.188×10^{-2}	0.254×10^{-2}	0.122×10^{-2}	0.129×10^{-2}	0.905×10^{-3}	0.203×10^{-2}	0.121×10^{-2}	0.245×10^{-2}	0.473×10^{-2}	0.320×10^{-2}
7.0–7.5	0.000×10^{0}	0.000×10^{0}	0.000×10^{0}	0.000×10^{0}	0.000×10^{0}	0.000×10^{0}	0.000×10^{0}	0.000×10^{0}	0.000×10^{0}	0.000×10^{0}	0.000×10^{0}
	0.169×10^{-1}	0.900×10^{-2}	0.225×10^{-2}	0.207×10^{-2}	0.107×10^{-2}	0.806×10^{-3}	0.494×10^{-3}	0.137×10^{-1}	0.102×10^{-2}	0.535×10^{-2}	0.186×10^{-2}

TABLE IV. Systematic errors. A summary of the contributions to the systematic error in the measured cross section (see text). If the components are uncorrelated and the errors add in quadrature, the overall systematic error is 5%. If the components are completely correlated and the errors add linearly, the overall systematic error is 13%. Since the errors are almost completely uncorrelated, the overall error of 8% quoted in the text is conservative.

Source	Error (%)
Counter and trigger efficiency	0.4
Trigger processor efficiency	1.0
Reconstruction efficiency	4.0
Resonance contamination correction	1.2
Reinteraction correction	2.0
Effective length	1.7
Acceptance	1.2
Beam normalization	1.5

tistical and the second is systematic. In addition, there is an uncertainty due to the A-dependence correction of $\pm 11\%$. A breakdown of the experimental systematic error is given in Table IV. For the differential cross sections, we estimate any additional relative systematic error between extreme values of the variables to be less than 10%.

At our beam momentum of 125 GeV/c, the total cross sections and the differential cross sections as functions of M and p_T^2 are very similar for the $\bar{p}$ and π^- data. However, the pion data exhibit a substantially flatter dependence on x_F $[=(x_1-x_2)/(1-\tau)]$, which is consistent with the harder momentum distribution of the valence quarks inside the pion as expected from counting rules.[28]

VI. COMPARISON OF $\bar{p}$ DATA TO THEORETICAL PREDICTIONS

In the leading-log approximation of QCD, the Drell-Yan cross section for hadronic production of dimuons integrated over p_T is given by (1) where the $q(x,Q^2)$'s are the quark structure functions of the beam and target particles. The structure functions needed in this equation should be identical to those measured in DIS with Q^2 identified as M^2. Figures 10(a) and 10(b) show the differential cross sections $d\sigma/dx_F$ (all p_T and $4<M<9$ GeV/c^2) and $d\sigma/dM$ (all p_T and $x_F>0$) for our $\bar{p}$ data. The solid curves are the predictions of (1) (after the appropriate integrations) obtained using structure functions from the QCD fit of Duke and Owens[29] (DO) with $\Lambda=0.2$ GeV (set 1) to neutrino, muon, and electron DIS data. The predictions have been multiplied by a factor of $K=2.41$ to obtain the measured total cross section. The valence-valence, valence-sea, sea-valence, and sea-sea components of the predictions are shown separately in Figs. 10(a) and 10(b). The valence-valence interaction accounts for 87% of the $\bar{p}$-produced cross section.

Figure 11 shows $d\sigma/dx_F$ and the first-order QCD prediction of Kubar *et al.*[7] The curve was calculated using

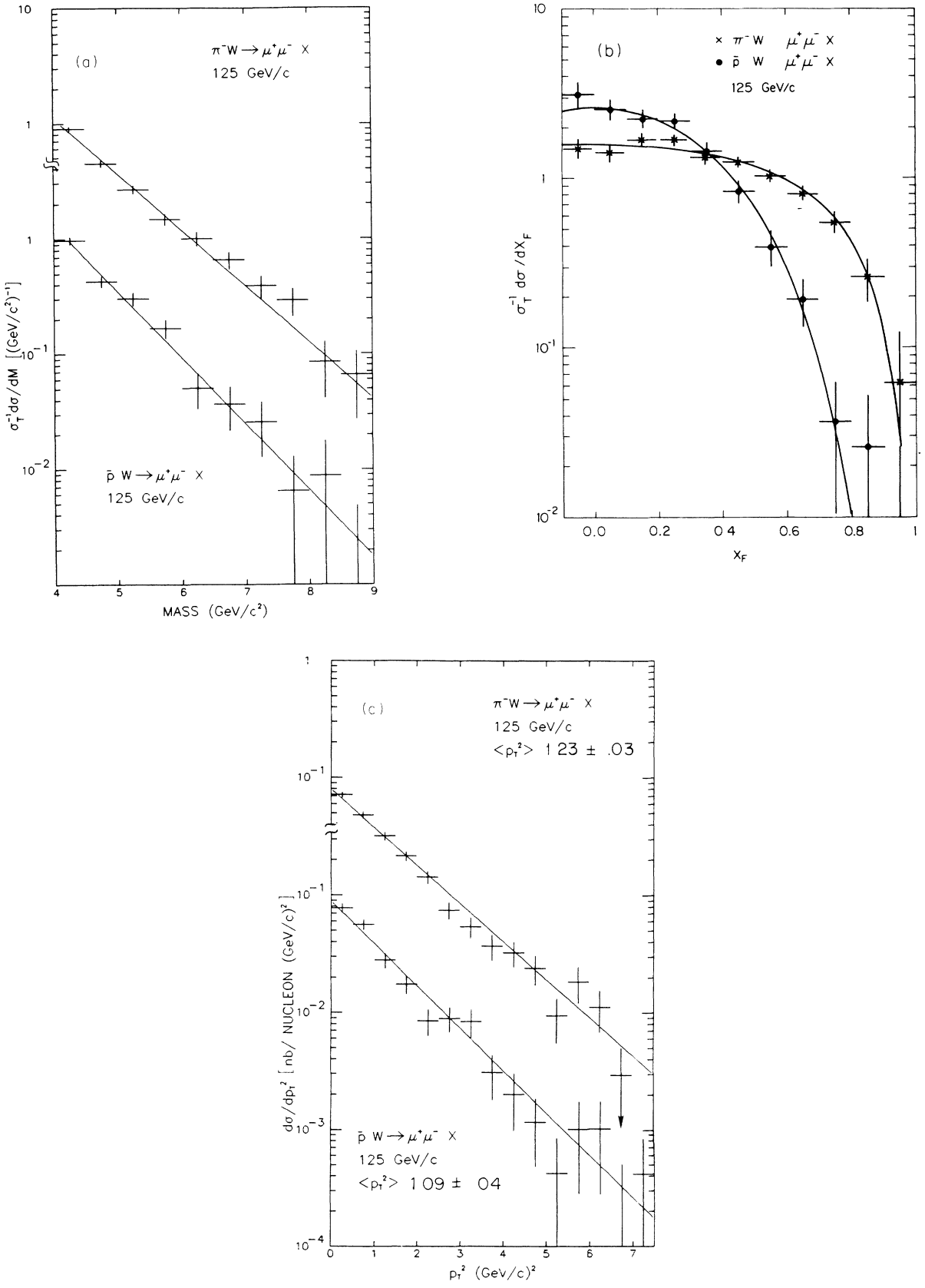

FIG. 9. The points show the (a) mass, (b) x_F, and (c) p_T^2 distributions for the $\bar{p}$-produced and π^--produced data. In the case of the mass and p_T^2 distributions, the vertical scale is broken and the $\bar{p}$ and π^- data offset by one decade to avoid excessive overlap. The curves are the predictions of the maximum-likelihood fits [Table II(b)].

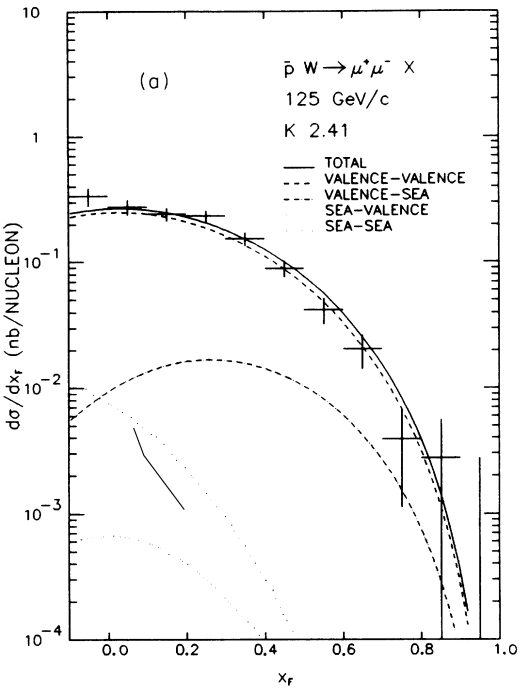

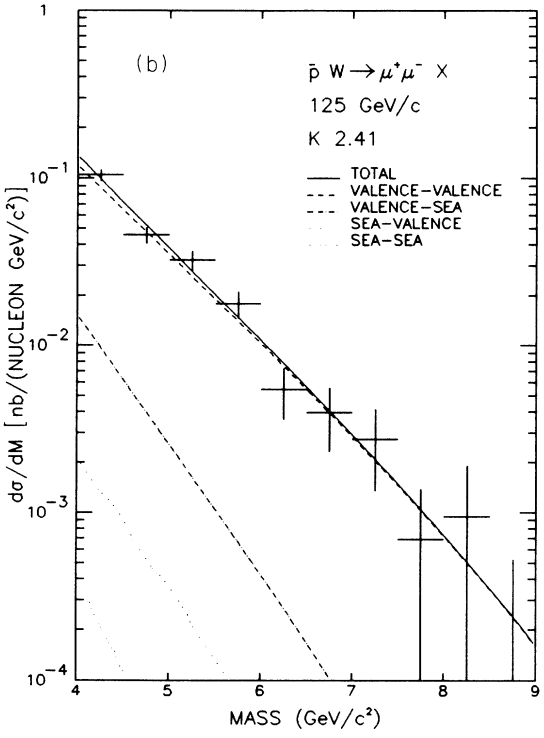

FIG. 10. The points show the (a) x_F and (b) mass distributions of the $\bar{p}$-produced data. The solid line shows the shape of the cross section predicted by the Drell-Yan model [leading-log approximation (LLA)] using DIS structure functions (Ref. 29) for both the $\bar{p}$ and nucleon. The curve has been multiplied by a factor of 2.41 to reproduce the measured total cross section for $4.0 < M < 9.0$ GeV/c^2 with $x_F > 0$. The other curves show the components of the predicted cross section as indicated.

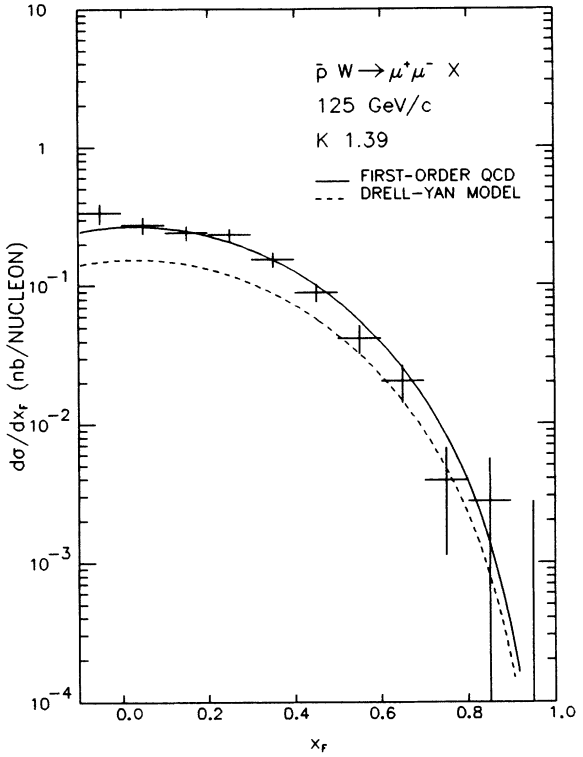

FIG. 11. The x_F distribution of the $\bar{p}$-produced data compared to the first-order QCD and Drell-Yan model (LLA) predictions. The curves have been multiplied by a factor 1.39, so that the first-order QCD prediction reproduces the measured total cross section for $4.0 < M < 9.0$ GeV/c^2 with $x_F > 0$.

$\Lambda = 0.2$ GeV and the structure functions of DO. It was multiplied by a factor of 1.39 to normalize to the measured total cross section ($x_F > 0$, all p_T, $4 < M < 9$ GeV/c^2) for our $\bar{p}$ data. Also shown in the figure is the naive Drell-Yan prediction multiplied by the same factor. The shapes of the leading-log and first-order calculations are almost identical and both are in good agreement with the data. Values of the ratio of the first-order to leading-log predictions are given as a function of x_F and M in Table V. It can be seen that this ratio is nearly constant over the kinematic range covered.

The ultimate accuracy of these comparisons is limited by several factors: (1) the statistical and systematic errors of our measurement; (2) the uncertainty in the A-dependence correction due to the error in the measured dimuon production A dependence and the related EMC effect measured in DIS data; (3) systematic differences among DIS experiments using the same target; and (4) the uncertainty in the value of Λ extracted from the fits of DO when used for first-order QCD calculations. The statistical and systematic errors in our measurement and the uncertainty in the A-dependence correction have already been described. We now consider the other two factors in more detail.

The DO structure functions[29] were derived from a simultaneous fit to data obtained with several different beams and targets. Appropriate (electromagnetic or weak) forms of $\int F_2(x)dx$ for the various data sets were compared in regions of Q^2 overlap, and all data were re-

TABLE V. First-order QCD corrections. The ratio of the first-order to leading-log-approximation cross sections for muon-pair production in $\bar{p}W$ collisions as a function of mass and x_F. The entries were calculated from formulas in Ref. 7 using the DIS structure functions of Duke and Owens (Ref. 29).

M \ x_F	0.0	0.1	0.2	0.3	0.4	0.5	0.6	0.7	0.8	0.9
4.0	1.725	1.727	1.727	1.726	1.722	1.716	1.707	1.695	1.679	1.654
4.5	1.734	1.735	1.736	1.735	1.733	1.729	1.722	1.714	1.703	1.687
5.0	1.744	1.746	1.747	1.747	1.746	1.743	1.740	1.735	1.728	1.720
5.0	1.757	1.759	1.760	1.760	1.760	1.759	1.758	1.756	1.754	1.754
6.0	1.771	1.773	1.774	1.775	1.776	1.777	1.777	1.778	1.781	1.788
6.5	1.787	1.789	1.791	1.792	1.794	1.796	1.798	1.802	1.808	1.822
7.0	1.805	1.807	1.809	1.811	1.813	1.816	1.820	1.826	1.836	1.857
7.5	1.825	1.827	1.829	1.831	1.834	1.839	1.844	1.852	1.866	1.893
8.0	1.847	1.849	1.851	1.854	1.858	1.863	1.870	1.881	1.897	1.930
8.5	1.872	1.874	1.876	1.879	1.884	1.890	1.899	1.911	1.931	1.970
9.0	1.899	1.901	1.903	1.907	1.912	1.920	1.930	1.945	1.968	2.013

normalized to agree with the μ-H_2 measurement of the EMC. Table VI lists the renormalization factors for data used in the structure function fits and for other data found in the literature.[30–32] There are systematic differences of roughly $\pm 5\%$ about the μ-H_2 data of the EMC which clearly cannot be attributed to an A dependence or EMC effect. An error of 5% in the normalization of the derived quark structure functions propagates to become a 10% uncertainty in the Drell-Yan-model predictions.

The first-order QCD calculation is also sensitive to the value chosen for Λ. Duke and Owens find a correlation between the value of Λ and the "hardness" of the gluon distribution used in their fit. They state that the DIS data alone cannot distinguish between $\Lambda=0.2$ GeV with a soft-gluon distribution (set 1) and $\Lambda=0.4$ GeV with a hard-gluon distribution (set 2). However, they note that the structure functions obtained using a soft-gluon distribution and $\Lambda=0.2$ GeV are in better agreement with another fit to DIS data,[33] and, when used in a simple hadroproduction model better predict the $pp \rightarrow \psi X$ cross section. Recently Martin *et al.*[34] have analyzed DIS experiments with the soft-gluon distribution and find best fits with $\Lambda=0.1$ GeV using EMC muon data and $\Lambda=0.2$ GeV using new Bologna-CERN-Dubna-Munich-Saclay (BCDMS) muon data. In this paper, we have used the $\Lambda=0.2$ GeV soft-gluon fits of Duke and Owens in our predictions and, specifically, $\Lambda=0.2$ GeV in the calculation of α_s for the first-order prediction. Using $\Lambda=0.4$ GeV increases the first-order prediction by 13% and using $\Lambda=0.1$ GeV decreases the first-order prediction by 8%. The choice of Λ has a significant effect on the QCD-predicted shape of the transverse-momentum distribution which will be examined in Sec. X.

To summarize, the normalization uncertainties that arise in the comparison of our data to the calculations are due to the statistical error ($\pm 5\%$) and systematic error ($\pm 8\%$) of our measurement, the uncertainty in the A-dependence correction ($\pm 11\%$), the DIS normalization uncertainty ($\pm 10\%$) and, in the case of the first-order prediction, the uncertainty in the value of Λ ($\pm 13\%$). Combining these errors in quadrature, we find that the leading-log prediction must be scaled by a factor $K=2.41\pm 0.42$ and the first-order prediction by a factor of 1.39 ± 0.30 to equal the measured total cross section for $x_F>0$ and $4<M<9$ GeV/c^2. The leading-log prediction is clearly too small and the first-order prediction is barely consistent with the measured cross section. The data can accommodate significant contributions from higher-order corrections.

A theoretically predicted K factor can be defined as the ratio of a higher-order cross section to the leading-log

TABLE VI. Normalization of DIS experiments. The relative normalizations of several high-statistics DIS experiments using various beams and targets. These were found by comparing appropriate forms of $\int F_2(x)dx$ where Q^2 overlaps in Refs. 29–32. The approximate fractional systematic error in each experiment is given in the last column.

Expt.	Beam	Target	EMC(μH_2)/Expt.	Expt. Sys. Error
EMC	μ	H_2	1	0.03
EMC	μ	Fe	1.03	0.03
EMC	μ	D_2	1.05	0.03
CDHS	ν	Fe	0.96	0.06
CCFRR	ν	Fe	0.94	0.06
BFP	μ	Fe	0.98	0.03
SLAC	e	H_2	0.92	0.03

value. For the first order in the $\bar{p}N$ interaction at 125 GeV/c, $K[O(\alpha_s)]=1.74$ if $\Lambda=0.2$ GeV and $K[O(\alpha_s)]=1.98$ if $\Lambda=0.4$ GeV. The major contribution to $K[O(\alpha_s)]$ is the so-called π^2 term which arises from gluon exchange at the $q\bar{q}$ vertex. The most singular part of this Drell-Yan vertex correction may be calculated to all orders in α_s, giving the following formula for an improved K factor:[35]

$$K(\text{vertex, all orders})=e^{(\alpha_s/2\pi)c_F\pi^2} \times\{K[O(\alpha_s)]-(\alpha_s/2\pi)c_F\pi^2\} ,$$

where $c_F=\frac{4}{3}$. Since the vertex correction dominates the first-order K factor, it has been argued[36,37] that K(vertex, all orders) may be a good approximation to the QCD prediction to all orders. For 125-GeV/c $\bar{p}N$ data K(vertex, all orders)=2.10 if $\Lambda=0.2$ GeV and K(vertex, all orders)=2.58 if $\Lambda=0.4$ GeV, both of which are in better agreement with the measured value of 2.41 than the first-order estimate.

There may be a contribution to the dimuon cross section above $M=4$ GeV/c^2 from charm or beauty decays. The best evidence against a large contribution to valence-valence–dominated processes such as $\pi^- N$ and $\bar{p}N$ is the experimental observation[3] that the ratio $\pi^- N/\pi^+ N$ approaches $\frac{1}{4}$ as expected for an electromagnetic process such as that of Drell-Yan instead of 1, which would be expected if the dimuons were the decay products of strongly produced $D\bar{D}$ or $B\bar{B}$ pairs. In addition, the polar decay angle distribution for the π^- is in good agreement with the Drell-Yan prediction of $1+\cos^2\theta$ as observed here and elsewhere.[3] The invariant-mass dependence of dimuons from charm or beauty decays is probably very different from that predicted by the Drell-Yan model. For example, Fisher and Geist[38] have shown that for light quark and gluon fusion the dimuon mass spectrum falls much faster than that of the Drell-Yan model for pp collisions. Using our $\bar{p}$ data we have calculated separate K factors for two mass bins, $4<M<5$ GeV/c^2 and $5<M<9$ GeV/c^2, and find $K=2.35\pm0.14$ and 2.51 ± 0.25, respectively, where the errors are statistical, indicating no strong variation with mass. This suggests that the contribution to the dimuon cross section from heavy-quark decays is small. Although the parton structure functions are known independently of the dimuon cross section in the case of $\bar{p}N$ interactions, it is very difficult to make a reasonably quantitative prediction of the heavy-quark contribution to the measured dimuon cross section due to the current experimental and theoretical uncertainties in the heavy-quark hadroproduction cross sections and production mechanisms.

VII. SCALING TESTS OF THE DRELL-YAN MODEL

In the naive quark-parton version of the Drell-Yan model, the cross sections $M^3 d^2\sigma/dM\,dx_F$ and $s^{3/2}d^2\sigma/dM\,dx_F$ should scale in terms of both variables τ and x_F. Figure 12 shows the cross section $M^3 d\sigma/dM$ with $x_F>0$ as a function of $\sqrt{\tau}$ for our antiproton data at 125 GeV/c and the data of the NA3 experiment[39] at 150

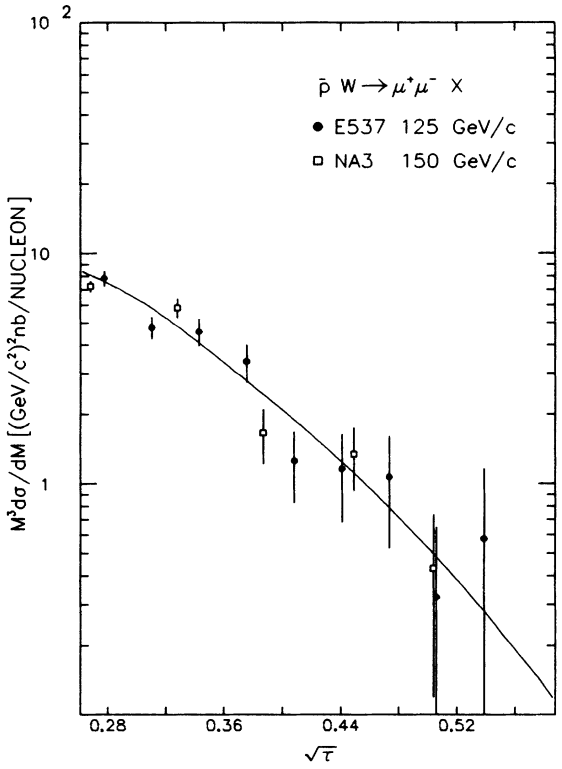

FIG. 12. $M^3 d\sigma/dM$ as a function of $\sqrt{\tau}$ for the $\bar{p}$-produced data in this experiment and for the data of Ref. 39 at 150 GeV/c. The solid curve is the prediction of the Drell-Yan model (LLA) integrated over $x_F>0$.

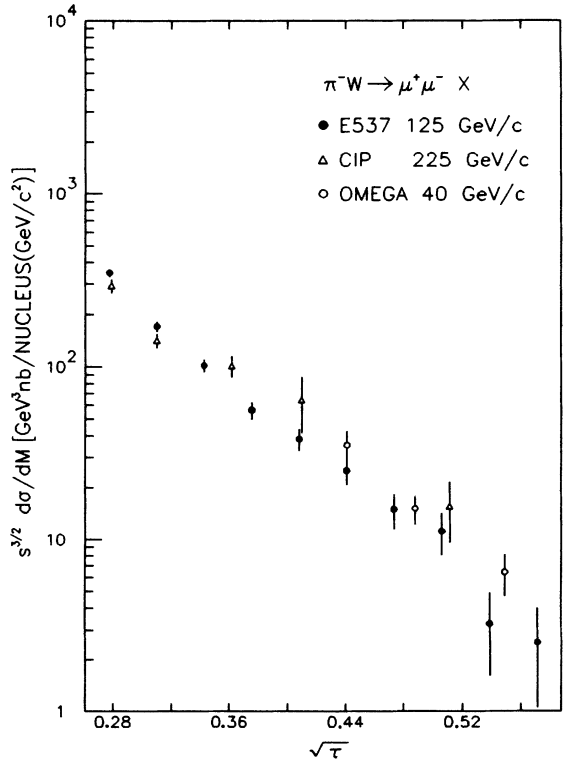

FIG. 13. Our measurement of the scaling cross section $s^{3/2}d\sigma/dM$ with $x_F>0$ for the production of muon pairs in $\pi^- N$ interactions is shown together with data obtained by the CIP (Ref. 40) and Omega (Ref. 41) Collaborations as a function of $\sqrt{\tau}$.

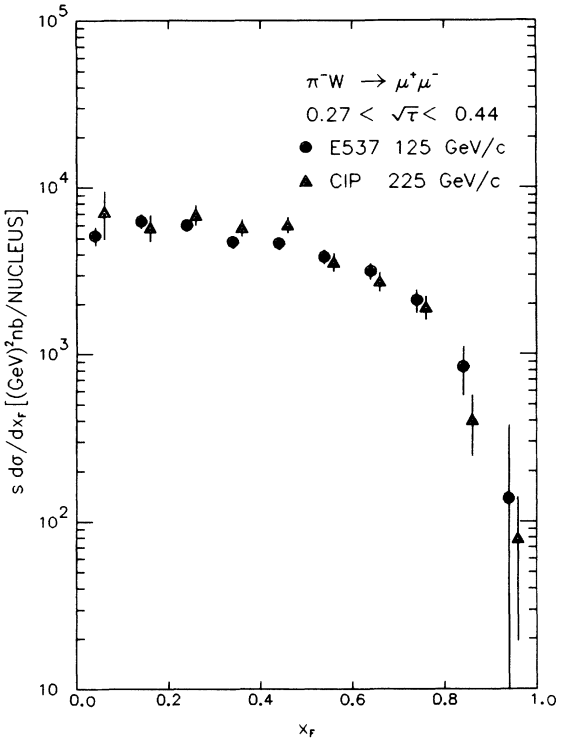

FIG. 14. Our measurement of the cross section $s\,d\sigma/dx_F$ for $0.27<\sqrt{\tau}<0.44$ compared to data obtained by the CIP Collaboration in the same region of $\sqrt{\tau}$.

GeV/c. The two measurements agree within errors and are consistent with the shape predicted by (1).

A more detailed scaling test can be made using data obtained with an incident π^- beam. Figure 13 shows the cross section $s^{3/2}d\sigma/dM$ with $x_F>0$ plotted versus $\sqrt{\tau}$ for our pion data, that of the Chicago-Illinois-Princeton (CIP) experiment[40] at 225 GeV/c, and that of the Omega experiment[41] at 39.5 GeV/c. Figure 14 shows the cross section $s\,d\sigma/dx_F$ in the range $0.27<\tau<0.44$ for our data and that of the CIP experiment. In both cases the data exhibit simple scaling. Note that the differential cross section $d\sigma/dx_F$ for our data at 125 GeV/c is smaller than the CIP data at 225 GeV/c by a factor of 1.8 whereas the cross section $s\,d\sigma/dx_F$ agrees within 15% over the full range of x_F covered.

VIII. QUARK STRUCTURE FUNCTIONS

In this section we present the extraction of the valence-quark structure functions for the $\bar{p}$ and π^- by fitting our data to (1). The statistical significance of the data is inadequate to extract quark structure functions that depend on both x and Q^2 so only the x dependence is considered. In the case of the antiproton, an estimate of the systematic error this introduces was made by assuming a Q^2 dependence similar to the Q^2-evolved DIS structure functions of DO (Ref. 29).

For antiprotons incident on a nuclear target, the individual beam and target quark structure functions in (1) may be written in terms of the valence-quark and sea-quark structure functions of the proton:

$$\begin{aligned}
&\bar{u}^{\bar{p}}=u_v^p+S^p,\quad \bar{d}^{\bar{p}}=d_v^p+S^p\ ,\\
&u^N=(Z/A)u_v^p+[1-(Z/A)]d_v^p+S^p\ ,\\
&d^N=(Z/A)d_v^p=[1-(Z/A)]u_v^p+S^p\ ,\\
&u^{\bar{p}}=d^{\bar{p}}=\bar{u}^N=\bar{d}^N=\bar{s}^{\bar{p}}=s^{\bar{p}}=s^N=\bar{s}^N=S^p\ .
\end{aligned}\tag{2}$$

Similarly, for incident pions the quark structure functions in (1) may be written in terms of valence and sea structure functions:

$$\begin{aligned}
&\bar{u}^{\pi^-}=d^{\pi^-}=V^\pi+S^\pi\ ,\\
&\bar{d}^{\pi}=\bar{s}^{\pi^-}=u^{\pi^-}=S^\pi\ .
\end{aligned}\tag{3}$$

The parametrizations used in the fits are

$$\begin{aligned}
&u_v^p(x)=a_p x^{\alpha_p}(1-x)^{\beta_p}\ ,\\
&d_v^p(x)=0.57u_v^p(x)(1-x)\ ,
\end{aligned}\tag{4}$$

and

$$V^\pi(x)=a_\pi x^{\alpha_\pi}(1-x)^{\beta_\pi}\ .$$

The relationship between u_v^p and d_v^p was that observed in deep-inelastic neutrino scattering data.[42] The sea distribution of the proton was taken from the DIS analysis of DO, and the sea distribution of the pion from fits to π^- and π^+ data of the NA3 Collaboration.[43] Recall that sea quarks contribute to only $\sim 13\%$ of the total cross section for the $\bar{p}N$ data.

The fits cannot distinguish between a constant K factor multiplying (1) and an increase of a_p and/or a_π. In the case of the $\bar{p}$, the K factor can be constrained to be the value found by comparing the data to the Drell-Yan prediction using DIS structure functions, but this is not possible for the π^--produced data. Fortunately, the normalization of the valence-quark structure functions can be constrained by other methods, which we will call the "number sum method" and the "momentum sum method." Independent K factors can then be extracted from the structure function fits using (1). As before, we define the K factor as the factor by which the Drell-Yan prediction must be increased to reproduce the experimental cross section for $4<M<9$ GeV/c^2 and $x_F>0$.

The number sum method (the method normally used in Drell-Yan fits to π^- data) requires the integral of the valence-quark distribution functions over all values of Bjorken x to equal the number of valence quarks in the hadron, that is,

$$\int_0^1[(u_v^p+d_v^p)/x]dx=3\ \text{ and }\ \int_0^1(2V^\pi/x)dx=2\ .\tag{5}$$

The major drawback of this method is that the dominant contributions to the integrals come from very small values of x, where the fixed-target experiments are not sensitive. Typical dimuon experiments produce data above $x_1=0.2$, while measurements of xF_3 in DIS (Refs. 30 and 44) as shown in Fig. 15 indicate that only $\sim\frac{1}{4}$ of $\int_0^1[(u_v^p+d_v^p)/x]dx$ lies above $x=0.2$. The number sum method clearly depends heavily on the extrapolation of the fitted structure function parametrization for $x>0.2$ to very small values of x. The choice of a different func-

tional form to parametrize the structure functions, for example, a sum of terms of the form $x^{\alpha}(1-x)^{\beta}$, could drastically alter the normalization of the calculated Drell-Yan cross section while still integrating over x to give the proper number of valence quarks.

The momentum sum method requires that the integral of the valence-quark structure function distributions over all x equals the momentum fraction carried by the valence quarks in the nucleon as measured in DIS at our average value of $Q^2=M^2=25$ GeV^2, and a similar expression for the pion, that is,

$$\int_0^1 (u_v^p+d_v^p)dx=0.34 \quad \text{and} \quad \int_0^1 2V^{\pi}dx=0.34 \ . \qquad (6)$$

The first integral in (6) was calculated using the $\Lambda=0.2$ GeV (set 1) solution of Ref. 29 for the valence-quark structure functions of the nucleon. The value of the integral decreases by 3.8% if the $\Lambda=0.4$ GeV (set 2) solution is used instead. The momentum sum method is certainly justified for the $\bar{p}$ data, but must be considered a plausible assumption for the π^- data. Because the factor of $1/x$ is lost in the integrand as compared to (5), the dominant parts of the integrals are now in the x range covered by the data and the normalization is much less sensitive to any extrapolation of the parametrization to small values of x.

Tables VII(a) and VII(b) give the results of several different fits of our $\bar{p}$ and π^- data to (1). These fits were made using all individual data events by the maximum-likelihood technique. All the π^- fits were made by constraining the target-quark distributions to be those of DO (Ref. 29). The $\bar{p}$ data were treated in this same way and also by fitting both the target- and beam-quark distributions simultaneously to the same quark structure function parametrizations. For each normalization method and target structure function constraint, the data were fitted both with α as a free parameter and with $\alpha=0.5$ as expected from Regge theory arguments.[45] No errors are listed for the fit K factors due to the uncertainty in normalizing the structure functions. The lower limit on the percentage errors is 17%, the value obtained from the comparison of our $\bar{p}$ data to the Drell-Yan prediction using structure functions from DIS.

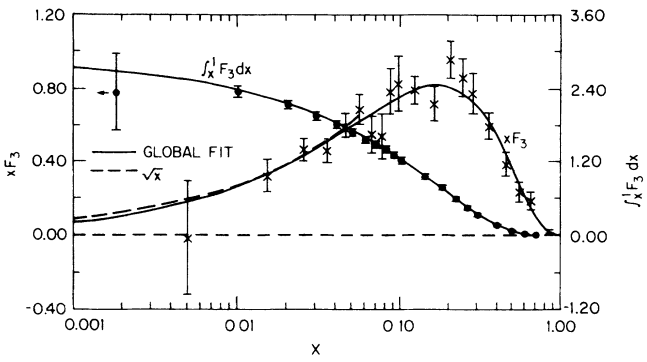

FIG. 15. xF_3 and $\int_x^1 xF_3 dx/x$ measured by the Caltech-Columbia-Fermilab-Rochester-Rockefeller (CCFRR) Collaboration (Ref. 30) at $Q^2=3$ GeV^2. Only $\sim\frac{1}{4}$ of $\int_0^1 xF_3 dx/x=\int_0^1 (u_v+d_v)/x\,dx$ lies above $x=0.2$.

A. Discussion of the $\bar{p}$ results

In fits 1–6 of Table VII(a), the beam-quark and target-quark structure functions were both fit to the same parametrization. Comparison of fit 1 with $\alpha=0.5$ and fit 2 with α free to vary illustrates the sensitivity of the K factor to the parametrization when using the number sum

TABLE VII. Structure-function parameters. Results of fitting the $\bar{p}$ and π^- valence-quark structure functions to the form $ax^{\alpha}(1-x)^{\beta}$ under various assumptions concerning the normalization and target structure function as described in the text. Angular brackets indicate that a parameter was fixed in the fit.

Fit	Target structure function	Norm method	α	β	K
		(a) $\bar{p}$			
1	Free	Num. sum	⟨0.5⟩	3.570±0.213	4.37
2	Free	Num. sum	0.678±0.211	3.711±0.274	2.37
3	Free	Mom. sum	⟨0.5⟩	3.574±0.213	3.01
4	Free	Mom. sum	0.685±0.253	3.717±0.294	2.60
5	Free	DIS	⟨0.5⟩	3.575±0.213	⟨2.41⟩
6	Free	DIS	0.677±0.027	3.710±0.300	⟨2.41⟩
7	DIS ($Q^2=M^2$)	DIS	⟨0.5⟩	3.421±0.195	⟨2.41⟩
8	DIS ($Q^2=M^2$)	DIS	0.701±0.558	3.622±0.608	⟨2.41⟩
9	DIS ($Q^2=25$)	DIS	⟨0.5⟩	3.456±0.196	⟨2.41⟩
10	DIS ($Q^2=25$)	DIS	0.640±0.558	3.580±0.611	⟨2.41⟩
		(b) π^-			
11	DIS ($Q^2=M^2$)	Num. Sum	⟨0.5⟩	1.291±0.077	2.43
12	DIS ($Q^2=M^2$)	Num. Sum	0.442±0.207	1.248±0.175	2.68
13	DIS ($Q^2=M^2$)	Mom. Sum	⟨0.5⟩	1.289±0.078	2.55
14	DIS ($Q^2=M^2$)	Mom. Sum	0.476±0.248	1.272±0.191	2.57

method normalization of (5). The K factors obtained from fits 3 and 4, which use the momentum sum method of (6), are much closer together and in reasonable agreement with the K factor found by comparing the data to the Drell-Yan prediction using DIS structure functions. The values of the parameters α and β are insensitive within errors to the normalization method used.

For fits 7–10 the target structure functions were constrained to be those of DO. Fits 7 and 8 allowed the structure functions to vary as a function of Q^2 and fits 9 and 10 fixed Q^2 to our mean value of 25 GeV^2. From the values of the parameters it can be seen that the fits are insensitive to the Q^2 evolution of the structure functions of the target quarks, which partially justifies the use of Q^2-independent parametrizations.

To illustrate the fits quantitatively and make comparisons with other data, (1) was manipulated to project out beam (B) and target (T) structure functions from the measured cross sections. For antiprotons, the equation can be written as

$$\frac{d^2\sigma}{dx_1dx_2}=K\frac{4\pi\alpha^2}{81}\frac{1}{x_1^2x_2^2}\left\{B(x_1,Q^2)T(x_2,Q^2)+\left[1-\frac{2Z}{A}\right]d_v^p(x_1,Q^2)[u_v^p(x_2,Q^2)-d_v^p(x_2,Q^2)]\right.$$
$$\left.+S^p(x_1,Q^2)\left[\left[1-\frac{3Z}{A}\right]u_v^p(x_2,Q^2)+\left[4-\frac{3Z}{A}\right]d_v^p(x_2,Q^2)+12S^p(x_2,Q^2)\right]\right\}, \quad (7)$$

where

$$B(x_1,Q^2)=4u_v^p(x_1,Q^2)+d_v^p(x_1,Q^2)\ ,$$
$$T(x_2,Q^2)=(Z/A)u_v^p(x_2,Q^2)+(1-Z/A)d_v^p(x_2,Q^2)$$
$$+S^p(x_2,Q^2)\ .$$

Here we have added an explicit K factor in our notation. As will be demonstrated shortly, the second and third terms on the right-hand side (RHS) of (7) contribute very little to the cross section and were calculated using the structure functions of Ref. 29. The beam and target structure functions can be calculated as averages over the $Q^2=M^2=sx_1x_2$ range of the data as follows:

$$B(x_1)=\int B(x_1,Q^2)T(x_2,Q^2)(1/x_2^2)dx_2$$
$$\times\left[\int T(x_2,Q^2)(1/x_2^2)dx_2\right]^{-1} \quad (8a)$$

and

$$T(x_2)=\int B(x_1,Q^2)T(x_2,Q^2)(1/x_1^2)dx_1$$
$$\times\left[\int B(x_1,Q^2)(1/x_1^2)dx_1\right]^{-1}. \quad (8b)$$

Figure 16 shows a plot of the values of $KB(x_1)$ which were found from (7) and (8a) using our measured cross sections $d^2\sigma/dx_1dx_2$ and the DO structure functions to calculate both $T(x_2,Q^2)$ and the small terms on the RHS of (7). The curves in the figure are the predictions using structure functions from fits 1 and 2 in Table VII(a) and from DO. The fits with $\alpha=0.5$ and α free to vary describe the data well for $x_1>0.2$ but give much different K factors. Recall that the fits ignored the Q^2 dependence of the quark structure functions. The predictions of $kB(x_1)$ using DIS structure functions with Q^2 evolution and with Q^2 fixed are almost identical and in good agreement with the data, indicating that the fits are good measurements of the $\bar{p}$ quark structure function at $Q^2=M^2=25$ GeV^2. Figure 17 again shows the values of $KB(x_1)$ for our experiment and the values for the $\bar{p}$ data of the NA3 Collaboration at 150 GeV/c (Ref. 39). There is excellent agreement between the two experiments.

Figure 18 shows the projected beam structure function and the predictions using the Duke and Owens structure functions both with and without considering the second and third terms on the RHS of (7). It is evident that these terms make only a small contribution to the predicted value.

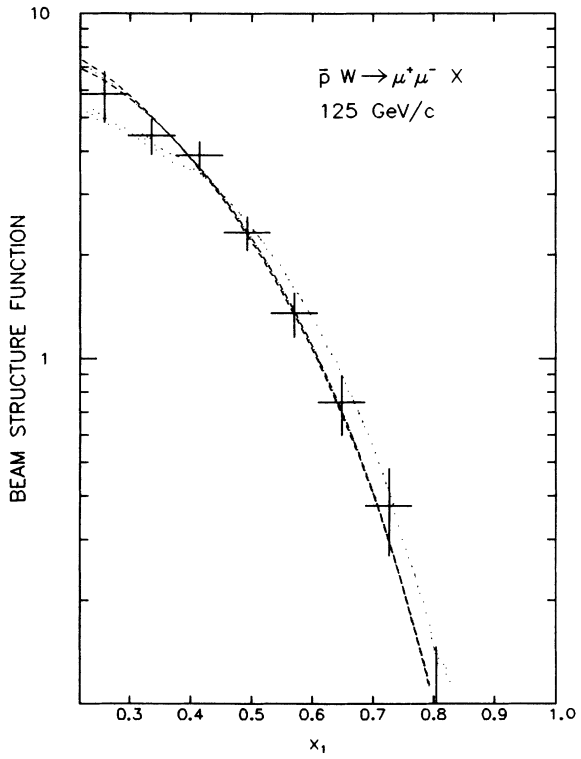

FIG. 16. The points are the projection of the beam structure function ($KB(x_1)=K[4u_v^p(x_1)+d_v^p(x_1)]$) for the $\bar{p}$ data. The dot-dashed line shows the prediction of fit 7 in Table VII, with α fixed to 0.5. The dashed line shows the curve corresponding to fit 8 with α free. The dot-blank line and the dotted line show the value of the deep-inelastic structure functions (Ref. 29) with $Q^2=M^2$ and with $Q^2=25$ GeV^2, respectively.

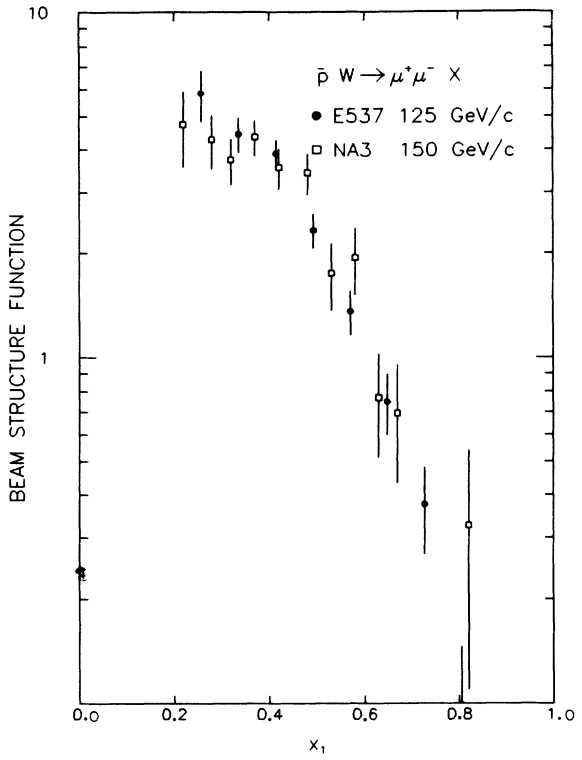

FIG. 17. Our projected $\bar{p}$ valence-quark structure function $[KB(x_1)]$ is compared with data obtained by the NA3 Collaboration (Ref. 39).

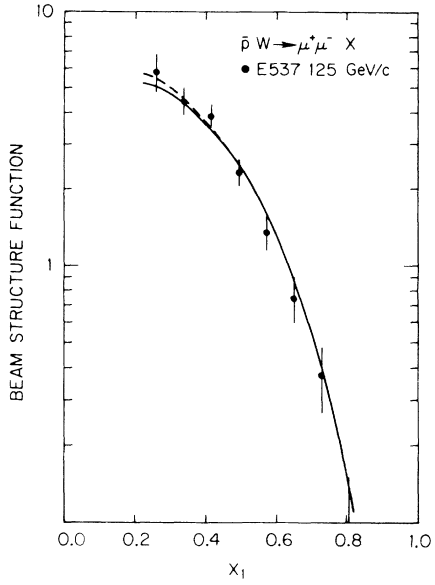

FIG. 18. The data points are the projected $\bar{p}$ beam structure function $[KB(x_1)]$. The solid curve is the prediction of the Drell-Yan model (7) using DIS structure functions (Ref. 29). The dashed curve is the prediction if one ignores the second and third terms on the RHS of (7), in which case the cross section can be written exactly as the product of a function of x_1 and a function of x_2.

Figure 19 shows a projection of $KT(x_2)$ using (7) and (8b). The DO structure functions were again used to calculate $B(x_1,Q^2)$ and the small terms on the RHS of (7). This projection is also consistent with the prediction based on DIS data although the range of x_2 is limited.

B. Discussion of the π^- results

The π^- fits in Table VII(b) were all made with the target quark distributions constrained to be those of Duke and Owens. The fits using the number sum method of (5) yield $K=2.43$ for $\alpha=0.5$ and $K=2.68$ for α free to vary. The K factors obtained from the momentum sum method fits are again almost equal with $K=2.55$ for $\alpha=0.5$ and $K=2.57$ for α free to vary. We believe that the momentum sum method gives a good estimate of the K factor with the assumption that the valence quarks in the pion carry the same fraction of the hadron momentum as the valence quarks in the nucleon. Note that the K-factor values obtained are very similar to the value of $K=2.41$ for the $\bar{p}$-produced data.

To project out the beam and target quark structure functions for the π^- data, (1) may be rewritten as

$$\frac{d^2\sigma}{dx_1dx_2}=K\frac{4\pi\alpha^2}{81}\frac{1}{x_1^2x_2^2}\left\{V^{\pi}(x_1,Q^2)T(x_2,Q^2)+S^{\pi}(x_1,Q^2)\left[\left[1+\frac{3Z}{A}\right]u_v^p(x_2,Q^2)+\left[4-\frac{3Z}{A}\right]d_v^p(x_2,Q^2)+11S^{\pi}(x_2,Q^2)\right]\right\}, \tag{9}$$

where

$$T(x_2,Q^2)=\frac{4Z}{A}u_v^p(x_2,Q^2)+4(1-Z/A)d_v^p(x_2,Q^2)+5S^p(x_2,Q^2)\ .$$

Figure 20 shows the values of $KV^{\pi}(x_1)$ which were projected by using in (9) the measured cross sections for $d^2\sigma/dx_1dx_2$, the results of Duke and Owens for the nucleon quark structure functions, and $S^{\pi}(x)=0.292(1-x)^{8.2}$ as measured by the NA3 Collaboration.[43] The Q^2 averaging was handled as in the $\bar{p}$ case by using (8a) and (8b). The curve in the figure represents the predictions of both fit 11 with $\alpha=0.5$ and fit 12 with α free to vary. Although the predictions for $x_1>0.2$ are identical, the K factors differ (2.43 compared to 2.68), which again indicates the sensitivity of the K factors obtained to the low-x behavior of the parametrization when using the number sum method of normalization.

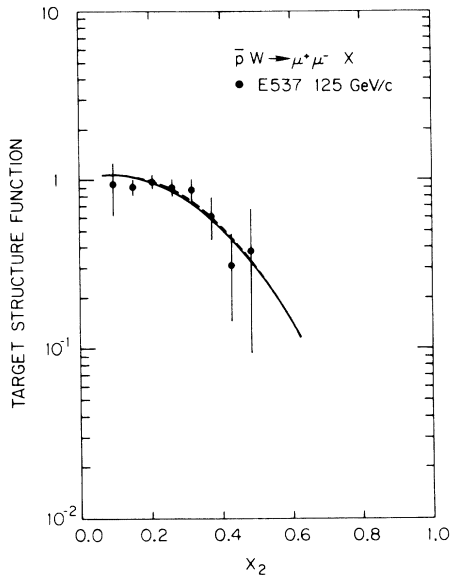

FIG. 19. The points are the projection of the target structure function $(KT(x_2)=K[Z/Au_v^p(x_2)+(1-Z/A)d_v^p(x_2)+S^p(x_2)])$ for the $\bar{p}$ data. The curve is the prediction of the Drell-Yan model using DIS structure functions (Ref. 29).

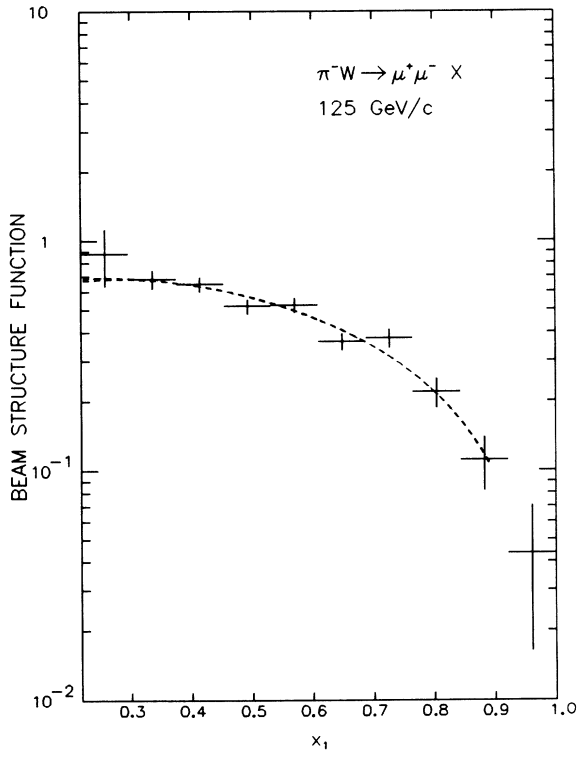

FIG. 20. The points are the projection of the beam structure function $[KV^{\pi}(x_1)]$ for the π^- data. The curve shows the pion valence-quark structure function fit using the parameters of either fit 11 of Table VII with α fixed to 0.5 or fit 12 with α free.

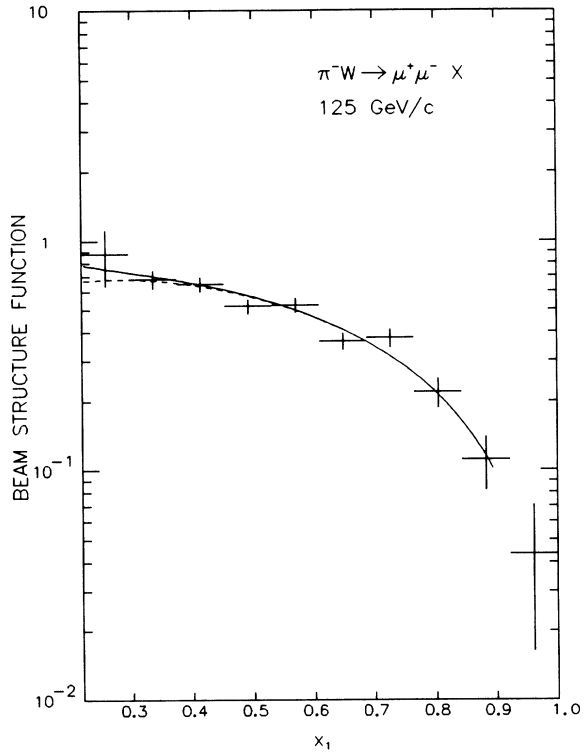

FIG. 21. The points are the projection of the beam structure function, $KV^{\pi}(x_1)$, for the π^- data. The dashed curve is the prediction of (9) using fit 11 of Table VII. The solid curve is the same prediction if one ignores the second term on the RHS of (9), in which case the cross section can be written exactly as the product of a function of x_1 and a function of x_2.

Figure 21 shows the projection of the beam structure function using the parameters of fit 12 and the same projection neglecting the second term on the RHS of (9). The effect of the second term is seen to be small, indicating that our results are insensitive to the sea-quark distribution in the pion.

Figure 22 shows the target structure function projection obtained from (9) and the prediction of DO using DIS data. There is good agreement over the complete range of x_2 covered. Figure 23 shows the values of the beam structure function $KV^{\pi}(x_1)$ for our experiment at 125 GeV/c, the NA3 experiment at 150 GeV/c (Ref. 43), the CIP experiment at 225 GeV/c (Ref. 46), and the Goliath experiment at 150 GeV/c (Ref. 47). The CIP data were multiplied by the ratio of $A^{1.12}/A^{1.0}$ so that the assumed A dependence is consistent with the other experiments. There is good agreement between all the data for values of x_1 approaching unity.

C. Effect of the first-order correction

In Table V we presented calculated values of $K[O(\alpha_s)]$ for the $\bar{p}W$ reaction as a function of x_F and M. Similar results were also obtained for the π^- reaction. It can be seen that the first-order correction has little variation over the kinematic range accessible to fixed-target experiments and will have a negligible effect on the variation

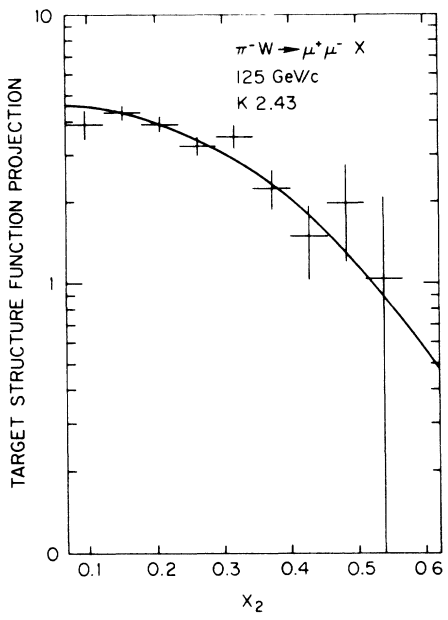

FIG. 22. The points are the projection of the target structure function $[KT(x_2)]$ for the π^- data. The curve is the prediction of the Drell-Yan model using DIS structure functions (Ref. 29).

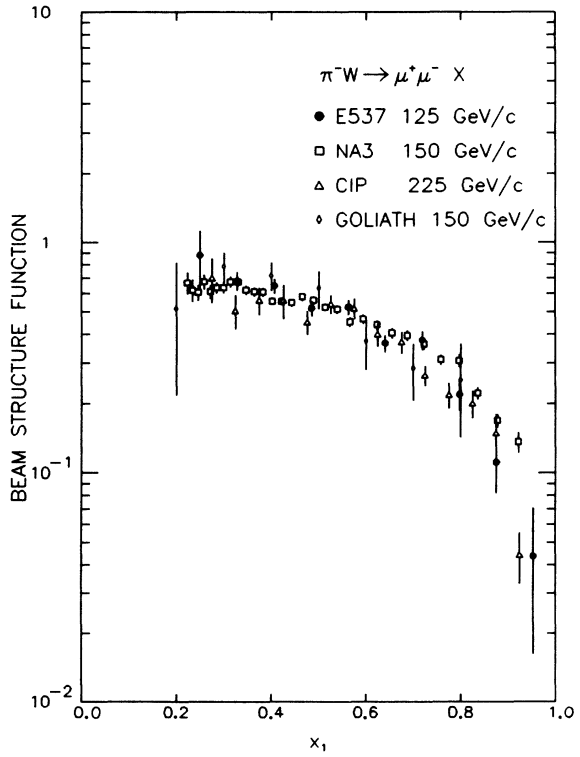

FIG. 23. Our projected pion valence-quark structure function $[KV^{\pi}(x_1)]$ compared with data from the NA3 (Ref.43), CIP (Ref. 46), and Goliath (Ref. 47) experiments. There is good agreement among the four experiments.

with x of the quark structure functions obtained from the present data.

IX. ANGULAR DISTRIBUTIONS

The angular distributions as functions of $\cos\theta$ and ϕ for the $\bar{p}$ and π^- data are shown in Figs. 24(a) and 24(b). Here θ and ϕ are the polar and azimuthal angles of the positive muon with respect to the beam direction in the dimuon rest frame. Superimposed on the $\cos\theta$ distributions is the simple Drell-Yan model prediction of $1+\cos^2\theta$. The data are consistent with the prediction except near $\cos\theta=-1$ where there are two experimental problems. First, the statistical accuracy of the data (especially the $\bar{p}$ data) is limited as $|\cos\theta| \rightarrow 1$ because the acceptance of the spectrometer falls to very low values (see Fig. 8). Second, the background due to accidental coincidences between high-momentum negative muons in the beam halo and low-momentum muons from hadron decay occurs near $\cos\theta=-1$ and gives rise to large fluctuations in the like-sign event background subtraction.

From Table II(a) it can be seen that the multidimensional fit with the parameter λ (in $1+\lambda\cos^2\theta$) free to vary gave $\lambda=1.1\pm0.3$ for the π^- data and $\lambda=0.3\pm0.4$ for the

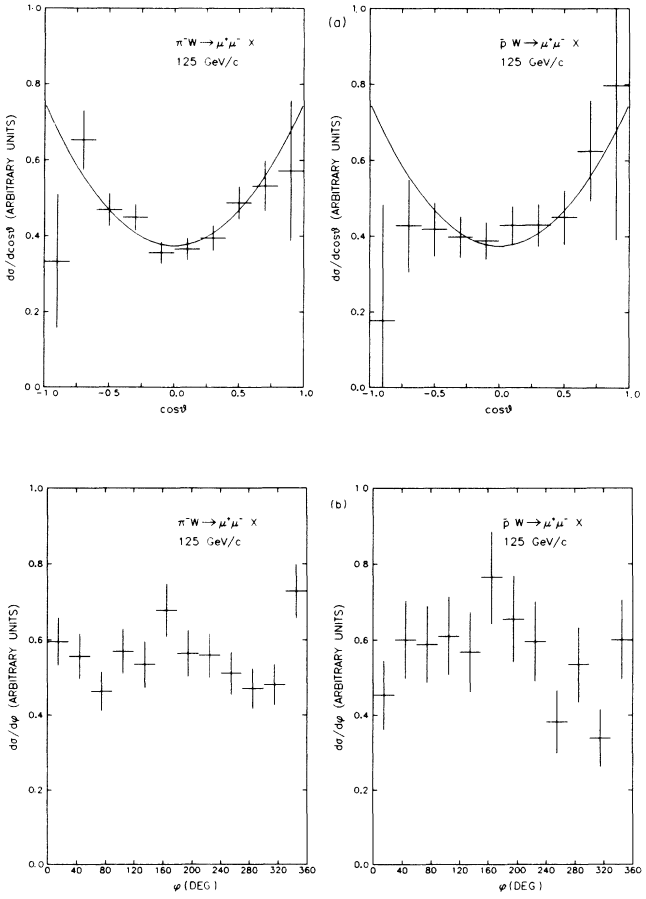

FIG. 24. The angular distributions for the $\bar{p}$ and π^- data in (a) $\cos\theta$ and (b) ϕ. The curves show the $1+\cos^2\theta$ prediction of the Drell-Yan model. Fluctuations from this prediction near $\cos\theta=-1$ may be caused by the remaining background and the like-sign subtraction as discussed in the text.

$\bar{p}$ data. Because of the limited acceptance and large background near $\cos\theta = -1$, we do not consider the $\bar{p}$ result to be in disagreement with the Drell-Yan model. In fact, for $\cos\theta > -0.5$ where there are no accidental background problems, both the $\bar{p}$ and π^- data closely follow the $1+\cos^2\theta$ prediction. The QCD corrections to the angular distributions[48] are too small to be meaningfully tested by this experiment. The cross sections presented here were therefore calculated assuming a uniform ϕ distribution and $\lambda = 1$. The only significant consequence of allowing λ to vary is to lower the absolute $\bar{p}$ cross section by 11%. The shapes of the differential cross sections are unaffected.

X. COMPARISON OF THE TRANSVERSE-MOMENTUM DISTRIBUTIONS WITH QCD

Many authors[9,49,50] have argued that there are contributions to the dimuon's transverse momentum from the following sources: (1) the intrinsic transverse momentum of the quarks inside the hadron; (2) the hard-scattering first-order annihilation and Compton graphs [see Figs. 1(c) and 1(d)] which are important for values of p_T near or in excess of the invariant mass; and (3) the emission of soft gluons for smaller values of p_T. Perturbative QCD cannot predict the contribution from the intrinsic transverse momentum of the quarks, so it must be extracted from data. We present two comparisons of the data to theoretical models which incorporate these contributions to p_T.

A. Comparison with the model of Chiappeta and Greco (Ref. 9)

In this treatment, the contributions of the first-order annihilation and Compton graphs to $\langle p_T^2 \rangle$ were calculated from Kubar *et al.*[7] and the soft-gluon emission predictions followed the treatment of Chiappetta and Greco,[9] who applied the leading-order and next-to-leading-order calculations of Kodaira and Trentadue[50] to compare with previously published dimuon data. The soft-gluon-emission contribution to the cross section may be written, following Ref. 9, as

$$\frac{d^3\sigma}{dM\,dx_F dp_T^2} = \frac{8\pi\alpha^2}{9M^3}\frac{1-\tau}{[x_F^2(1-\tau)^2+4\tau]^{1/2}}\int bJ_0(bp_T)\exp[S(b,M)]db \times \sum_{q=u,d,s} e_q^2[\bar{q}^B(x_1,Q^2)q^T(x_2,Q^2)+q^B(x_1,Q^2)\bar{q}^T(x_2,Q^2)] , \quad (10)$$

where

$$S(b,M) = -(2c_F/\pi)\int_{1/b}^{M}(dq_T/q_T)\{\ln(M^2/q_T^2)\alpha(q_T)[1+\kappa\alpha(q_T)/2\pi]+2\ln(e^{\gamma_E}/2)\alpha(1/b)-\tfrac{3}{2}\alpha(q_T)\} \quad (11)$$

with $\kappa = 3(\frac{67}{18}-\pi^2/6)-N_F(\frac{10}{18})$, $\gamma_E = 0.5772$ (Euler's constant), $N_F = 4$ (the number of active quark flavors), $c_F = \frac{4}{3}$, and

$$\alpha(q)/\pi = [12/(33-2N_F)][1/\ln(q^2/\Lambda^2)]-72[(153-19N_F)/(33-2N_F)^3]\{\ln[\ln(q^2/\Lambda^2)]/\ln^2(q^2/\Lambda^2)\} . \quad (12)$$

Equation (11) is only valid in the perturbative region where $b \ll 1/\Lambda$ and nonperturbative effects are parametrized by a regularization of $\alpha(q)$, which is accomplished by the substitution of $q^2+q_0^2$ for q^2 in (12). The value of q_0 used in this analysis was 1.0 GeV. The intrinsic transverse momentum was introduced by inserting an additional factor of $\exp(-b^2\langle p_T^2\rangle_{\rm int}/4)$ into the integrand of (10).

The QCD calculations were made using the DIS structure functions of DO (Ref. 29) for the nucleon and the structure functions of Owens[51] for the π^-. Some double counting occurred by directly summing the soft-gluon and annihilation contributions to $\langle p_T^2 \rangle$, but since the latter is small (see Figs. 26 and 27 below) the results should not be significantly altered by a more complete treatment.

Figures 25(a)–25(d) show the differential cross sections $d\sigma/dp_T^2$ with $4 < M < 9$ GeV/c^2 and $x_F > 0$ for our $\bar{p}$ and π^- data. We find average p_T^2 values of 1.09 ± 0.04 (GeV/c)^2 for the $\bar{p}$ data and 1.23 ± 0.03 (GeV/c)^2 for the π^- data. The soft-gluon-emission and intrinsic quark transverse-momentum contributions to $d\sigma/dp_T^2$ for $\Lambda = 0.2$ GeV and $\langle p_T^2\rangle_{\rm int} = 0.3$, 0.4, 0.5, 0.6, and 0.7 (GeV/c)^2 are shown in Figs. 25(a) and 25(b). The predictions for $\Lambda = 0.4$ GeV and $\langle p_T^2\rangle_{\rm int} = 0.5$ (GeV/c)^2 are shown in Figs. 25(c) and 25(d). In all cases the predictions were normalized to the integrated cross section, so only shape comparisons of theory to data are meaningful. Note that smaller values of $\langle p_T^2\rangle_{\rm int}$ are required in order to fit the data as Λ increases. Without invoking the first-order annihilation and Compton diagrams, the p_T^2 dependence of the data is described well out to 5 (GeV/c)^2.

Comparing the $\langle p_T^2 \rangle$ of our total data sample with $4 < M < 9$ GeV/c^2 and $x_F > 0$ to predictions with $\Lambda = 0.2$ GeV which include contributions from both soft-gluon and hard processes gives $\langle p_T^2\rangle_{\rm int} = 0.4$ (GeV/c)^2 for the $\bar{p}$ data and 0.3 (GeV/c)^2 for the π^- data. Slightly negative $\langle p_T^2\rangle_{\rm int}$ values are actually required for predictions with $\Lambda = 0.4$ GeV.

The predictions of $\langle p_T^2 \rangle$ as functions of both M and x_F are shown with the data in Figs. 26 and 27. In order to minimize computer time, the predictions versus M were made at the average x_F of the data and the predictions versus x_F were calculated at the average M^2. The figures show that the hard contribution is much smaller than the soft-gluon contribution in this region. The rise in $\langle p_T^2 \rangle$ with increasing values of M observed in other data and predicted at higher energies[9] is not pronounced at 125 GeV/c. The predictions agree fairly well with the data except in the highest-mass bins of the pion sample.

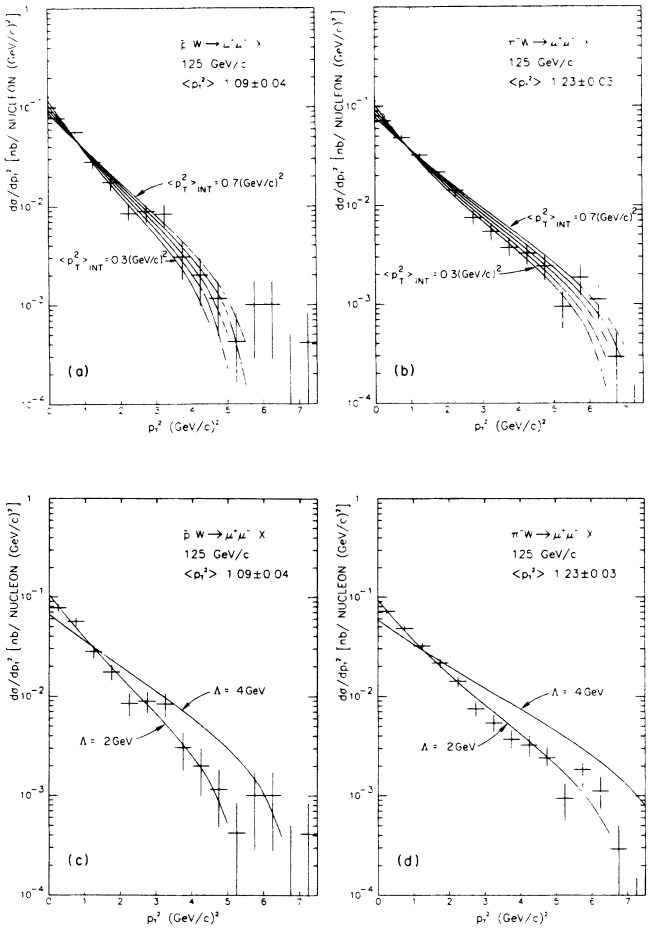

FIG. 25. $d\sigma/dp_T^2$ for the $\bar{p}$ and π^- data. The curves are the predictions of the soft-gluon model of Chippetta and Greco (Ref. 9) including an intrinsic p_T^2. (a) and (b) show the predictions of the model for $\Lambda=0.2$ GeV and $\langle p_T^2\rangle_{\rm int}=0.3$, 0.4, 0.5, 0.6, and 0.7 $(\mathrm{GeV}/c)^2$. (c) and (d) show the predictions for $\Lambda=0.2$ and 0.4 GeV using $\langle p_T^2\rangle_{\rm int}=0.5\ (\mathrm{GeV}/c)^2$.

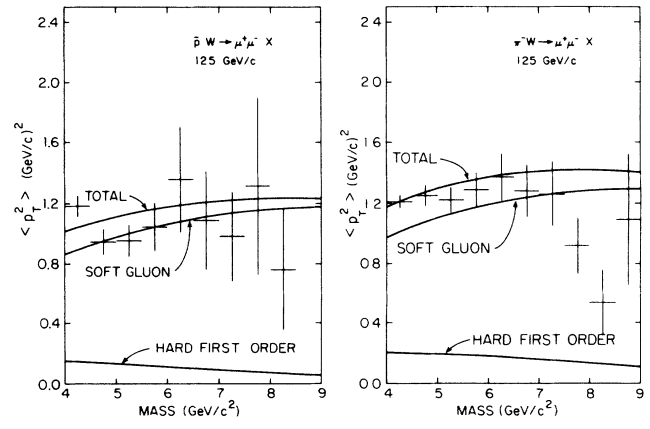

FIG. 26. $\langle p_T^2\rangle$ vs M for $\bar{p}$ and π^- data. The curves are the total and component QCD predictions of Chiappetta and Greco (Ref. 9) as indicated, calculated at the average x_F of the data.

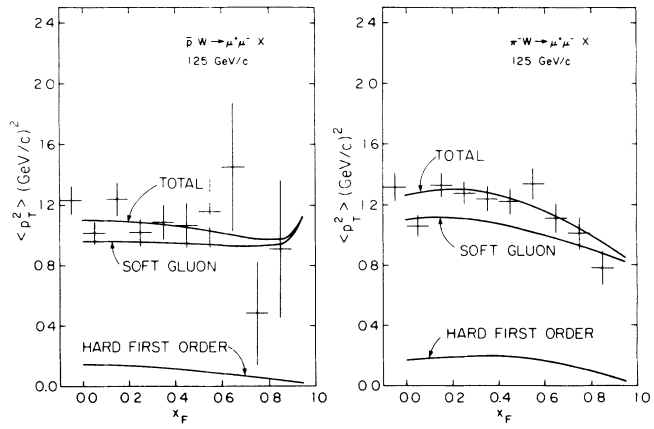

FIG. 27. $\langle p_T^2\rangle$ vs x_F for $\bar{p}$ and π^- data. The curves are the total and component QCD predictions of Chiappetta and Greco (Ref. 9) as indicated, calculated at the average M^2 of the data.

B. Comparison with the model of Altarelli *et al.* (Ref. 52)

The calculation of the differential cross section $d\sigma/dp_T^2$ of Altarelli *et al.*[52] addressed the problems that no absolute normalization could be predicted and that the singular $O(\alpha_s)$ Compton and annihilation contributions had to be arbitrarily cut off at low p_T. The model was developed to predict the p_T spectrum for W bosons produced at $p\bar{p}$ colliders. The triple differential cross section is given by

$$\frac{d\sigma}{dM\,dy\,dp_T^2}=\frac{4\pi\alpha^2}{9Q^2S}\left[\int\frac{d^2\mathbf{b}}{4\pi}\exp(-\mathbf{b}p_T)\times\exp[S(b^2,Q^2,y)]R(b^2,Q^2,y)+Y(p_T^2,Q^2,y)\right], \tag{13}$$

where α is the electromagnetic coupling constant, $\mathbf{b}$ is a two-dimensional vector in parameter space, Y is the $O(\alpha_s)$ contribution to the cross section coming from the Compton and annihilation graphs, from which the singular part at $p_T=0$ has been subtracted and added into R, S is the two-loop form factor coming from the all orders resummation of double logarithms, and finally R is the infrared sensitive part of the cross section. The cross section (13) was constructed to reproduce the first-order prediction[7] previously discussed in Sec. VI when integrated over transverse momentum. We have verified that this is true to within 6%, which is consistent with the estimated error in the numerical integration.

In Fig. 28(a) we compare $d\sigma/dp_T^2$ for our $\bar{p}$ data to the predictions of (13) integrated over M and y. The predictions used the structure functions of DO (Ref. 29) and were made with (a) set 1, $\Lambda=0.2$ GeV and $\langle p_T^2\rangle_{\rm int}=0$, (b) set 2, $\Lambda=0.4$ GeV and $\langle p_T^2\rangle_{\rm int}=0$, and (c) set 1, $\Lambda=0.2$ GeV and $\langle p_T^2\rangle_{\rm int}=0.5\ (\mathrm{GeV}/c)^2$. In Fig. 28(b) we com-

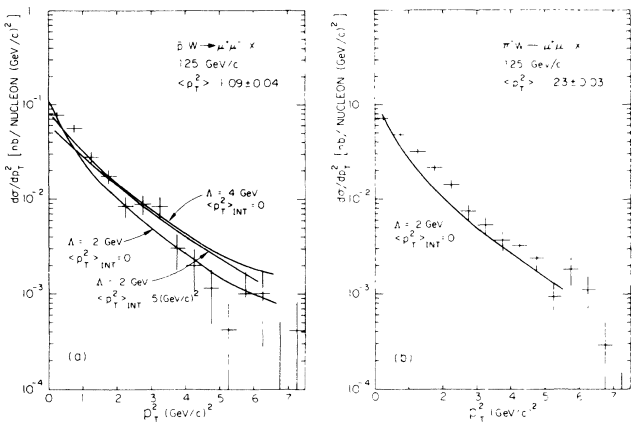

FIG. 28. $d\sigma/dp_T^2$ for the (a) $\bar{p}$ and (b) π^- data. The curves are the predictions of Altarelli *et al.* (Ref. 52).

pare $d\sigma/dp_T^2$ for our π^- data to the prediction of (13) using pion quark structure functions from the NA3 experiment[43] and the nucleon quark structure functions from DO with set 1, $\Lambda=0.2$ GeV and $\langle p_T^2\rangle_{\text{int}}=0$. As in the previous model, we see a considerable flattening of the prediction as Λ or $\langle p_T^2\rangle_{\text{int}}$ increases.

XI. SUMMARY AND CONCLUSIONS

We have studied the production of muon pairs with invariant mass between 4 and 9 GeV/c^2 in $\bar{p}N$ and π^-N interactions at an incident momentum of 125 GeV/c using a tungsten target. A tertiary beam containing 18% antiprotons allowed us to study the antiproton-induced reaction with higher statistics and smaller systematic errors than were obtained in previous experiments. Differential cross sections as functions of the dimuon invariant mass, Feynman x, transverse momentum, and the decay angles of the dimuon were obtained. The total cross sections, p_T distributions, and invariant-mass distributions for the $\bar{p}$- and π^--produced data are remarkably similar. However, the x_F distributions are different, reflecting the differences in the quark structure functions of the two beam particles.

The data have been compared to the QCD-improved Drell-Yan model and to calculations including higher-order QCD corrections. The $\bar{p}$ data are particularly valuable because dimuon production is dominated by the valence-valence interaction and the structure functions that must be used have been measured in deep-inelastic scattering. Most of the features of the data are consistent with simple Drell-Yan model calculations except that these must be multiplied by K factors to reproduce the absolute values of the measured cross sections. For the $\bar{p}$ data the value of K obtained was 2.41 ± 0.42. For the π^- data the best value of K was 2.57, but relied on constraining the normalization of the pion valence-quark distribution by the "momentum sum method." Various scaling distributions used to compare our results with other data, and the dimuon decay-angle distributions are also consistent with a simple Drell-Yan model. The net effect of higher-order QCD calculations is to leave the various distributions substantially the same, but progressively lower values of the K factors are needed to reproduce the data as the calculations are made more sophisticated.

We have extracted structure functions for the valence quarks in the $\bar{p}$ and π^- which are valid for $Q^2=M^2=25$ GeV^2 and for $x>0.2$. The results are in good agreement with dimuon data at other energies and with the nucleon quark structure functions obtained from DIS data.

The transverse-momentum distributions have been compared to QCD calculations including soft-gluon emission and the hard-scattering first-order annihilation and Compton scattering graphs. From the comparisons using the model of Chiappetta and Greco[9] with $\Lambda=0.2$ GeV we obtained average values of the squares of the intrinsic transverse momenta of the quarks inside the respective hadrons of 0.4 (GeV/c)^2 for the $\bar{p}$ and 0.3 (GeV/c)^2 for the π^-. For both the $\bar{p}$ and π^- data, the model gives a good description of the differential cross sections as a function of p_T^2, and of the dependence of $\langle p_T^2\rangle$ on M and x_F. The p_T^2 dependence of the data is described well out to 5 (GeV/c)^2 by the soft-gluon and intrinsic p_T^2 contributions without invoking the first-order annihilation and Compton diagrams.

ACKNOWLEDGMENTS

We thank the staff of the Fermilab Research Division, especially Garvie Hale and Karen Kephart, for their support in the construction and operation of the experiment. We also thank Chris Quigg of the Fermilab Theory Department for his valuable advice during the analysis. This work was performed at Fermi National Accelerator Laboratory and supported by the U.S. Department of Energy, the North Atlantic Treaty Organization Scientific Affairs Division, the International Programs and High Energy Physics Divisions of the National Science Foundation, the Natural Sciences and Engineering Research Council of Canada, the Quebec Department of Education, and the Hellenic Science and Technology Agency.

*Present address: University of Colorado, Boulder, Colorado 80309.
†Present address: Prairie View A&M University, Prairie View, Texas 77445.
‡Present address: Tata Institute, Bombay, India.
§Present address: Fermilab, Batavia, Illinois 60510.
**Present address: Cornell University, Ithaca, New York 14853.
††Present address: University of Chicago, Chicago, Illinois 60637.
‡‡Present address: Institute of High Energy Physics, P.O. Box 918, Beijing, People's Republic of China.
§§Present address: Shell Oil, Houston, Texas 77002.

[1] S. D. Drell and T. M. Yan, Phys. Rev. Lett. **25**, 316 (1970).
[2] I. R. Kenyon, Rep. Prog. Phys. **45**, 1261 (1982).

[3]E. Berger *et al.*, in *Proceedings of the Workshop on Drell-Yan Processes,* Batavia, Illinois, 1982 (Fermilab, Batavia, IL, 1983).
[4]E. Anassontzis *et al.*, Phys. Rev. Lett. **54**, 2572 (1985).
[5]H. Politzer, Nucl. Phys. **B129**, 301 (1977).
[6]W. Lindsay *et al.*, Phys. Rev. Lett. **117B**, 105 (1982).
[7]J. Kubar *et al.*, Nucl. Phys. **B175**, 251 (1980).
[8]P. K. Malhotra, in *Proceedings of the Workshop on Drell-Yan Processes* (Ref. 3); B. Cox and P. K. Mulhotra, Phys. Rev. D **29**, 63 (1984).
[9]P. Chiappetta and M. Greco, Nucl. Phys. **B199**, 77 (1982); **B221**, 269 (1983).
[10]E. Anassontzis *et al.*, Nucl. Instrum. Methods **A242**, 215 (1986).
[11]H. Areti *et al.*, Nucl. Instrum. Methods **212**, 135 (1983).
[12]J. Branson *et al.*, Phys. Rev. Lett. **38**, 1334 (1977), and references therein.
[13]C. Richard-Serre, CERN Report No. 71-18, 1971 (unpublished).
[14]C. Serre, CERN Report No. 67-5, 1967 (unpublished).
[15]P. M. Joseph, Nucl. Instrum. Methods **75**, 13 (1969).
[16]G. Koizumi, Fermilab Report No. TM-786, 1978 (unpublished).
[17]W. Schappert, Ph.D. thesis, McGill University, Montreal, 1984.
[18]A. Van Ginneken, Fermilab Report No. FN-272, 1975 (unpublished).
[19]L. Lyons, Prog. Part. Nucl. Phys. **7**, 169 (1981).
[20]For example, see R. Roy and B. Nigam, *Nuclear Physics* (Wiley, New York, 1967) for a discussion of the Fermi-gas model.
[21]E. Moniz *et al.*, Phys. Rev. Lett. **26**, 445 (1971).
[22]A. Bodek and J. Ritchie, Phys. Rev. D **23**, 1070 (1980).
[23]W. Eadie *et al.*, *Statistical Methods in Experimental Physics* (North-Holland, Amsterdam, 1971).
[24]K. Gottfreid and J. D. Jackson, Nuovo Cimento **33**, 309 (1964).
[25]A. S. Carroll *et al.*, Phys. Lett. **80B**, 319 (1979).
[26]G. Farrar, Phys. Lett. **56B**, 185 (1975).
[27]P. Bordalo *et al.*, Phys. Lett. B **193**, 368 (1987).
[28]S. Brodsky and G. Farrar, Phys. Rev. D **11**, 1309 (1975); Phys. Rev. Lett. **31**, 1153 (1973).
[29]D. Duke and J. Owens, Phys. Rev. D **30**, 49 (1984).
[30]R. E. Blair *et al.*, in *Novel Results in Particle Physics (Vanderbilt, 1982),* proceedings of the 5th International Conference on Particle Physics, Nashville, Tennessee, 1982, edited by R. S. Panvini, M. S. Alam, and S. E. Csorna (AIP Conf. Proc. No. 93) (AIP, New York, 1982), p. 250.
[31]A. R. Clark *et al.*, Phys. Rev. Lett. **51**, 1826 (1983).
[32]W. Krasny, in *Proceedings of the International Europhysics Conference on High Energy Physics,* Bari, Italy, 1985, edited by L. Nitti and G. Preparata (Laterza, Bari, 1985).
[33]H. Abramowicz *et al.*, Z. Phys. C **12**, 289 (1982).
[34]A. D. Martin *et al.*, Report No. DTP/8812, 1988 (unpublished).
[35]W. J. Sterling, in *Proceedings of the Workshop on Drell-Yan Processes* (Ref. 3), p. 131.
[36]G. Parisi, Phys. Lett. **90B**, 295 (1980).
[37]G. Curic and M. Greco, Phys. Lett. **92B**, 175 (1980).
[38]H. G. Fischer and W. M. Geist, Z. Phys. C **19**, 159 (1983).
[39]J. Badier *et al.*, Phys. Lett. **96B**, 422 (1980).
[40]C. Newman, Ph.D. thesis, University of Chicago, Chicago, 1979.
[41]M. J. Corden *et al.*, Phys. Lett. **96B**, 411 (1980).
[42]F. Eisele, in *Proceedings of the 21st International Conference on High Energy Physics,* Paris, France, 1982, edited by P. Petiau and M. Proneuf [J. Phys. Paris Colloq. **43**, C-3, Suppl. 12 (1982)].
[43]J. Badier *et al.*, Z. Phys. C **18**, 281 (1983).
[44]J. G. H. de Groot *et al.*, Z. Phys. C **1**, 143 (1979).
[45]G. Farrar, Nucl. Phys. **B77**, 429 (1974).
[46]G. E. Hogan *et al.*, Phys. Rev. Lett. **42**, 948 (1979).
[47]R. Barate *et al.*, Phys. Rev. Lett. **43**, 1541 (1979).
[48]John C. Collins, Phys. Rev. Lett. **42**, 291 (1979).
[49]J. C. Collins *et al.*, Nucl. Phys. **B250**, 199 (1985).
[50]J. Kodaira and L. Trentadue, Phys. Lett. **112B**, 66 (1982).
[51]J. F. Owens, Phys. Rev. D **30**, 943 (1984).
[52]G. Altarelli *et al.*, Nucl. Phys. **B246**, 12 (1984); Z. Phys. C **27**, 617 (1985).